AGU PUBLICATIONS

JGR

Journal of Geophysical Research: Solid Earth

RESEARCH ARTICLE
10.1002/2014JB011315

Key Points:
- Planform shape of gravity flows modeled by Rankine flow equations
- Rankine number (either fixed or transient) characterizes plume shapes
- Natural flows start with fast initial fluxes followed by decline

Supporting Information:
- Readme
- Movie S1
- Movie S2
- Movie S3
- Movie S4
- Movie S5
- Movie S6
- Movie S7
- Movie S8

Correspondence to:
R. Weijermars,
R.Weijermars@TUDelft.nl

Citation:
Weijermars, R., T. P. Dooley, M. P. A. Jackson, and M. R. Hudec (2014), Rankine models for time-dependent gravity spreading of terrestrial source flows over subplanar slopes, *J. Geophys. Res. Solid Earth*, *119*, doi:10.1002/2014JB011315.

Received 12 JUN 2014
Accepted 19 AUG 2014
Accepted article online 23 AUG 2014

Rankine models for time-dependent gravity spreading of terrestrial source flows over subplanar slopes

R. Weijermars[1,2,3], T. P. Dooley[1], M. P. A. Jackson[1], and M. R. Hudec[1]

[1]Bureau of Economic Geology, University of Texas at Austin, Austin, Texas, USA, [2]Department of Geoscience and Engineering, Delft University of Technology, Delft, Netherlands, [3]Alboran Energy Strategy Consultants, Delft, Netherlands

Abstract Geological mass flows extruding from a point source include mud, lava, and salt issued from subsurface reservoirs and ice from surface feeders. The delivery of the material may occur via a salt stock, a volcanic pipe (for magma and mud flows), or a valley glacier (for ice). All these source flows are commonly skewed by a superposed far-field velocity vector imposed by the topographic slope and thus develop plumes having a wide range of shapes. The morphological evolution of the perimeter of the plumes (in plan view) can be simulated by varying the key parameters in a simple analytical flow description on the basis of Rankine equations. Our model systematically varies the strength of the point source relative to the downslope far-field velocity of its expelled mass. The flow lines are critically controlled by the relative speed of the two rates, which can be concisely expressed by the dimensionless Rankine number (*Rk*, introduced in this study). For steady flows, plume widths can be expressed as a function of *Rk*. The viscosity of the rock, mud, or lava mass involved in the gravity flow affects *Rk* and thus the appearance of the plumes. For unsteady source strength, *Rk* becomes time dependent and the plume width varies over time. The model flow shapes suggest that the plume shapes of natural gravity flows of terrestrial surface materials (mud, lava, salt, and ice) commonly express fast initial flux of the source, followed by an exponential decline of the source strength. Flows having initially higher *Rk* but otherwise equal life cycles create broader plumes. Peaks in the source flux due to magmatic pulsing during the eruption cycle can explain the formation of pillow lavas. Rather than instantaneously reaching full strength before declining, some natural source flows start by swelling slowly, leading to the creation of unique plume shapes like a flying saucer.

1. Introduction

We develop a gravity flow model using potential theory to describe the planform evolution of high-viscosity fluids issued from a point source onto planar, solid surfaces, perfectly horizontal or with a slope. Potential flow theory can be directly applied, without any adaptations, to many flows involving incompressible, viscous fluids subjected to irrotational flow [*Joseph and Liao*, 1994; *Joseph*, 2003, 2006; *Joseph et al.*, 2007; *Weijermars*, 2014]. The frequently encountered misperception that potential flow descriptions would only apply to inviscous fluids probably follows from an overly cautious approach: inviscous fluids will always flow in irrotational fashion—even when boundaries are present—and therefore automatically fulfill the requirements of potential flow. *Joseph* [2006] emphasized that irrotational flow is a property of the flow; viscosity is a property of the material. Consequently, irrotational flows may occur in both viscous and inviscous fluids. An independent mathematical proof of potential flow as a scalable description of irrotational flow in viscous fluids (incompressible) is given in Appendix A.

Major examples of viscous or viscoplastic gravity flows of terrestrial surface materials from point sources include the crystalline creep of salt and ice in glaciers. Ice glaciers and salt glaciers are both composed of crystalline rocks which very high flow resistance follows from effective viscosity estimates of 10^{12}–10^{17} Pa s for ice [*Marshall*, 2005] and 10^{15}–10^{19} Pa s for salt [*Van Keken et al.*, 1993; *Wagner and Jackson*, 2011]. Both materials are practically incompressible when deposited and compacted into dense crystalline layers. The initial condition of flow onset is given by a certain discharge from a point source as that occurs in nature when buried rock salt is pressurized by geological forces and flows onto the surface from a salt stock to form salt glaciers (Figure 1). The feeder stock is in our study approximated by a point source. In the case of ice glaciers, the source region is a firn basin filled by snowfall before being compacted and flowing downslope similar to a salt glacier. When

©2014. American Geophysical Union. All Rights Reserved.

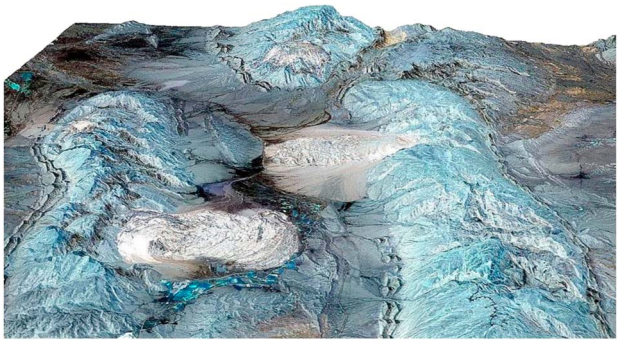

Figure 1. Salt glaciers (white flows) in central Zagros Mountains (Iran). Highly pressurized infra-Cambrian Hormuz salt rose up diapiric stocks in core of Miocene anticlines. Field of view 50 by 50 km looking due east. ASTER satellite image (false color, acquired in 2001) draped over digital elevation model. Gach diapir, foreground, 27.56°N, 54.47°E; Siah Tagh diapir, middle ground, 27.51°N, 54.57°E. (Image: http://asterweb.jpl.nasa.gov/gallery/images/salt-iran-view.jpg.)

valley glaciers exit a mountain range, they flow out onto a broad, unconfined plain to become a so-called piedmont glacier. Elephant Foot Glacier (Greenland) is a piedmont glacier and provides a pristine example of a fan-shaped gravity flow (Figure 2a). The shapes of relatively unconstrained terminal tongues of ice glaciers on Axel Heiberg Island tend to be more elongated (Figure 2b). Piedmont glaciers are built when the glacier leaves its channel vent and is allowed to spread over a relatively flat plane to form a wide fan or plume. The upstream valley is the feeder of the piedmont glacier's source flow.

The kinematics of aforementioned geological gravity flows are generally similar, but a wide variety of plume-like shapes is observed. Our aim is to determine how the key flow parameters (slope/viscosity/source strength) affect the geometric evolution of gravity flows in 2-D top views. The mass flow sets on when material is issued from the feeder with strength m onto the planar slope and is unable to resist downslope creep due to the gravitational pull. Crystalline ice and salt bodies both behave essentially as power law fluids at high stresses but become Newtonian when stresses are low. This means that no flow resistance exists when a deviatoric stress results in the downslope direction. The source strength may either be steady or time dependent. We explore the effect of both steady and time-dependent source strength on the geometry of the perimeter of the gravity flow. Any fluid issued with a certain strength m will be carried off faster by a low-viscosity fluid than by a high-viscosity fluid. Consequently, lower viscosity fluids tend to develop mass flows that move in thin streaks down a planar slope, while higher-viscosity fluids are carried off more slowly and thus the superposed slope flow has less effect on the perimeter expansion of the source flow. High-viscosity sources on a planar slope therefore can be expected to more readily evolve into broader fans rather than thin streaks (assuming similar slopes). In all cases considered here, the geological media have viscosities high enough to ensure that the gravity flow remains within the range of very low Reynolds numbers ($Re < 1$). This means that such flows show parabolic velocity profiles, which becomes apparent when height of the fluid is exaggerated relative to horizontal extent in vertical cross sections (Figure 3a). The lateral change in the thickness of such very low Re gravity flows is controlled by a scaling parameter α (see section 2.1). The class of gravity currents that develop hydraulic jumps farther away from the flow source (Figure 3b) is not considered here; such jumps are restricted to flows involving inertia effects ($Re > 1$) [*Bush et al*., 2006; *Huppert*, 2006; *Slim and Huppert*, 2011]. Turbulent gravity currents at $Re > \sim 10^3$ (Figure 3c) are also excluded from our analysis (for details on such gravity currents see *Hacker et al*. [1996] and *Birman and Meiburg* [2006]).

We discuss our simplifying assumptions (section 2), outline the Rankine model equations (section 3), and visualize the flow simulations (sections 4 and 5) followed by a discussion of the implications for the interpretation of geological flows (section 6). Our conclusions are presented in section 7.

2. Previous Research, Model Design, and Basic Assumptions

2.1. Previous Research (2-D Analytical Models of Vertical Sections)

Analytical models of gravity flows having low Reynolds number based on similarity solutions of subaerial gravity currents have used a scaling parameter, α, which can be used to characterize the vertical flow profiles of source flows [*Huppert*, 1982a; *Fletcher* et al., 1995]. The global continuity equation is [*Huppert*, 2006]

$$\int_0^{R_{N(t)}} (2\pi r)^n h(r,t)\mathrm{d}r = Qt^{\alpha} \quad \left[\mathrm{m}^3\right] \tag{1a}$$

©2014. American Geophysical Union. All Rights Reserved.

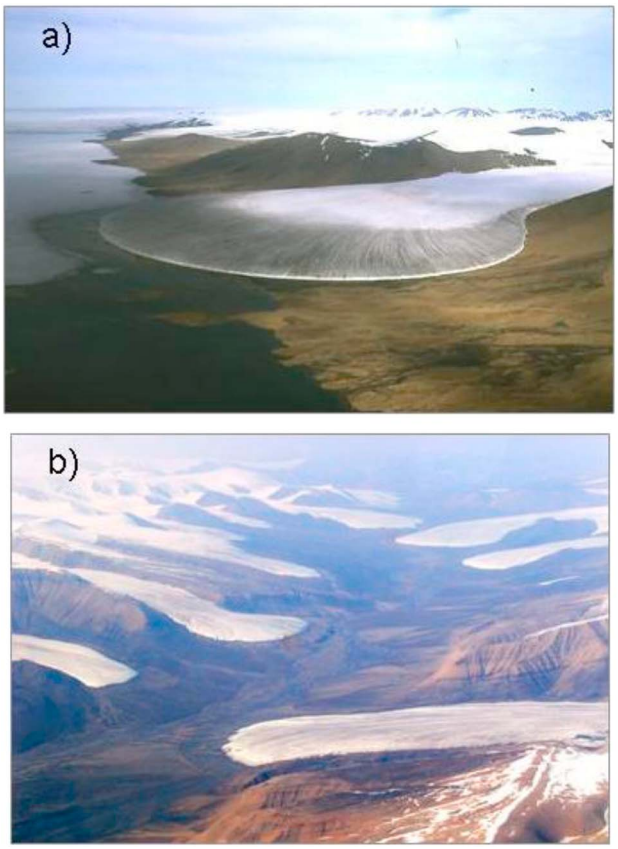

Figure 2. Piedmont ice glaciers. (a) Elephant Foot Glacier, photographed in July 1997 at 81°N on east coast of Greenland (courtesy Philippe Huybrechts). (b) Ice glaciers at Axel Heiberg Island in summer 2004 (courtesy Martin Jackson).

with flux, Q, time, t, radial position, r, layer height, h, and horizontal extent, $R_N(t)$, of the flow front. Integer $n = 1$ for axisymmetric gravity flows and $n = 0$ for 2-D flows. The flow profile is controlled by the flux of the source that supplies the fluid for the gravity spreading. The source flux, Q, at any time, t, is given by [*Fletcher* et al., 1995]

$$Q(t) = \alpha K_\alpha t^{\alpha-1} \quad \left[\mathrm{m}^3\ \mathrm{s}^{-1}\right] \qquad (1b)$$

where constant K_α is a dimensional measure of initial source strength and α is a positive nondimensional number. Figures 4a–4d highlight the various shapes of gravity flows spreading onto a flat horizontal surface for different α values. For $\alpha = 0$, no fluid volume is added from the source (which is a spreading salt sheet when applied to halokinesis; Figure 4a). This situation has been termed the "dam-break problem" or "mass slumping" [*Betelu et al.*, 1997]. It corresponds to the sudden spread of a gravity current after a constant volume of stored fluid is instantaneously released (so that $Q = 0$) [*Huppert and Simpson*, 1980]. For $\alpha = 1$, a steady state flow profile occurs with the flux, Q, remaining constant (Figure 4b). The gravity flow expands but does not change height above the source. For each specific viscosity fluid, the cross-sectional shape of the gravity current is determined by the balance between the source flux and the viscous resistance to spreading. Radial pressure drops steadily toward the unconstrained outer edge of the fluid, which has a certain thickness and mass [*Didden and Maxworthy*, 1982]. For $\alpha < 1$, the region above the flux source thins as the gravity current wanes (Figure 4c).

For $\alpha > 1$, a dynamic bulge grows above the flux source (Figure 4d), as modeled by *Huppert* [1982a]. The dynamic bulge is a viscous fountain supported by the dynamic pressure of rising fluid. In summary, for $\alpha = 1$, the flow is approximately steady state and the topographic profile widens but maintains the same height. For all other conditions, flow profiles are transient: for $\alpha > 1$, the spreading flow thickens over time; for $0 \leq \alpha < 1$, the spreading flow thins over time. Examples of waning and waxing flux sources on a slope ($\alpha < 1$ and $\alpha > 1$) where gravity currents carry the fluid downslope have been modeled by *Lister* [1992].

2.2. Laboratory and Analytical Flow Setup, Basic Assumptions (No Slope)

A physical model was constructed supplying a silicone polymer using a pump that issued the silicone via a feeder onto a flat, horizontal surface (Figures 5a and 5b). The fluid flux accelerated ($\alpha > 1$) during the model stages contoured in Figure 5a. The flux acceleration is indicated by the evenly spaced time contours mapped using multiple images of the base of the spreading fluid as time progressed; even spacing requires accelerating flux for the ever-increasing perimeter to advance. These contours of spreading rate fit well with those implied by $\alpha > 1$ models of both *Huppert* [1982a] and *Fletcher* et al. [1995]. The continuous advance of the 3-D viscous spreading of the fluid is similar to that in Figure 4d.

The viscous fountain model for $\alpha > 1$ shows a prominent dynamic bulge (Figure 5a), which was earlier modeled analytically by *Huppert* [1982a] and smoothed by *Fletcher* et al. [1995]. Both studies concede that the near-apex shape of the bulge suffers from unstable solutions. The presence of a dynamic bulge is a useful

©2014. American Geophysical Union. All Rights Reserved.

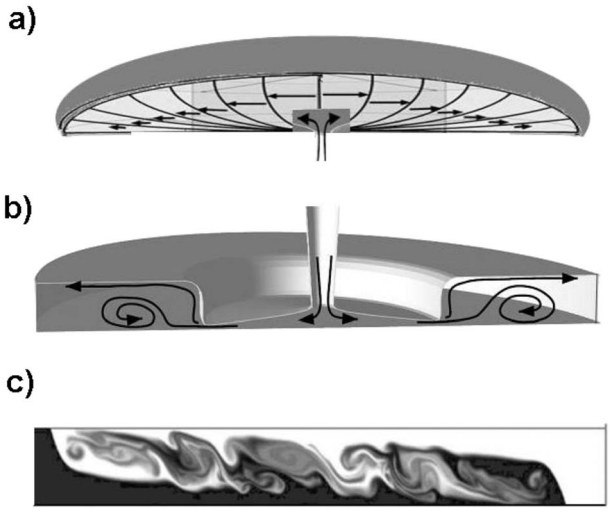

Figure 3. Three modes of gravity currents: (a) Laminar flow ($Re < 1$), (b) laminar flow with a peripheral hydraulic jump ($1 < Re < \sim 1000$), and (c) turbulent flow ($Re > \sim 1000$). (Figure 3b image after *Bush et al.* [2006] and Figure 3c after *Birman and Meiburg* [2006].)

clue to gravity flows over flat surfaces fed by geological fluids at unknown fluxes, Q, and is a common feature of active subaerial salt glaciers in Iran [*Talbot*, 1998]. We emphasize that a dynamic bulge requires an accelerating source supply rate ($\alpha > 1$). Such dynamic bulges will disappear after a supply source starts to wane ($\alpha < 1$) or dies ($\alpha = 0$). This ebbing phase has also been simulated in our physical model. Figure 5b shows the viscous relaxation of the bulge after the source flow was cut ($\alpha = 0$). Unlike the accelerating flux in Figure 5a, the waning flux in Figure 5b shows time contours that bunch together as the flow ebbs and the viscous fountain evolves into a viscous droplet.

This bunching of time contours for the source flow periphery displacement also occurs for axisymmetric source flows having constant flux. The ever-expanding

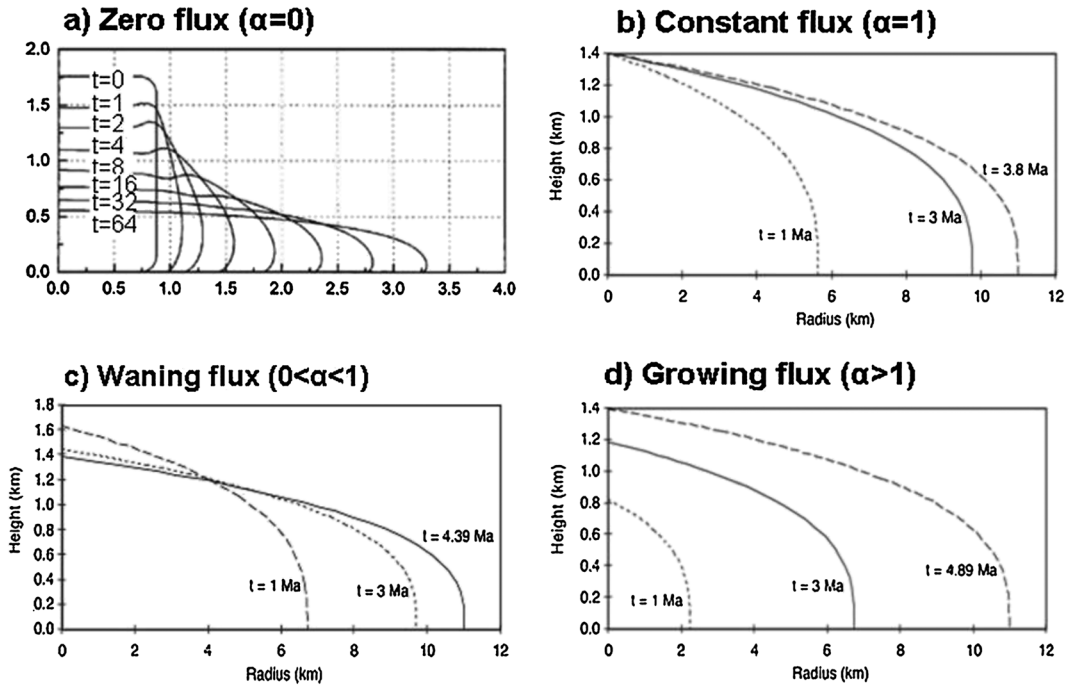

Figure 4. Diagnostic evolution of gravity flow profiles ($Re < 1$) for various flux rates based on 2-D gravity current models. (a) Dam-break gravitational collapse with zero strength of source flux ($\alpha = 0$). Basal velocity decelerates exponentially, and the layer thinning takes infinitely long; all units are nondimensional. (b) Steady state strength of source flux ($\alpha = 1$), where the basal velocity declines as function of radial spread, but the height of the layer remains constant once steady state flow profile is established. (c) Waning strength of source flux ($\alpha < 1$), where both basal velocity and height of layer vary at rates intermediate between Figures 4a and 4b. (d) Growing strength of source flux ($\alpha > 1$), where basal velocity may become constant or even accelerate depending upon rate of flux increase. Height of layer will continue to increase as long as the source flux grows. Note that vertical scale is exaggerated in Figures 4b–4d, and Figure 4a starts out with artificial height (Figure 4a after *Betelu et al.* [1997] and Figures 4b–4d after *Fletcher* et al. [1995]).

©2014. American Geophysical Union. All Rights Reserved.

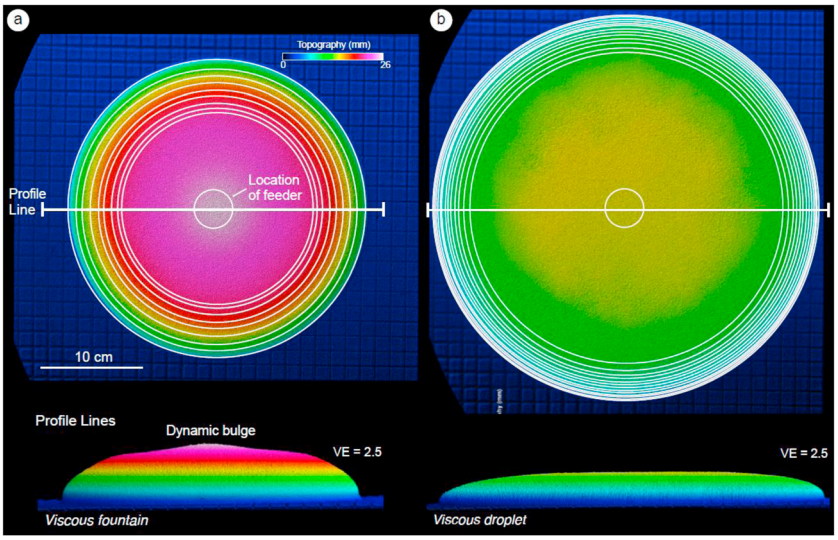

Figure 5. Planform and cross-section views of silicone (viscosity 5×10^4 Pa s [*Weijermars*, 1986, 1988]) spreading from source onto horizontal surface in physical model. Radial velocity components (u_r) were mapped with digital image laser scanning device using time series of 80 images. A thin dusting of ceramic microspheres was sifted onto the upper surface of the transparent silicone in order to get a return from the laser scanner. (a) Dynamic bulge of source flow with $\alpha > 1$ due to increasing flux rate. (b) Relaxation of silicone droplet after switching off the source flux so that $\alpha = 0$. The white circles in Figures 5a and 5b are isochrons showing advance of the spreading fluid for equal time intervals. Vertical exaggeration (VE) is 2.5.

circumference of the constant flow causes the radial velocity to decline. The timeline contours for the advancing outline of a radial expanding 2-D source flow with a constant source flux ($\alpha = 1$) are mapped in Figure 6. Any flux change immediately translates to a lateral velocity change in the thin layer approximation due to the exclusion of height changes.

The analytical model of a 2-D source flow can approximate the vertically averaged velocity profile for certain 3-D gravity flows onto a flat, horizontal surface with constant flux Q (Figure 6). The simplifying assumption of a 2-D flow neglects any changes in height h of the fluid bulge occurring in a 3-D flow, essentially a Hele-Shaw cell flow, the limitations of which are discussed in section 2.5. In the absence of a slope, the fluid expelled from the 2-D source spreads radially, and when the flux strength, Q, is steady, the radial velocity declines with the radial distance to the source by $Q/2\pi hr$. When layer thickness h remains constant throughout the layer, the farther the source fluid travels, the slower it flows.

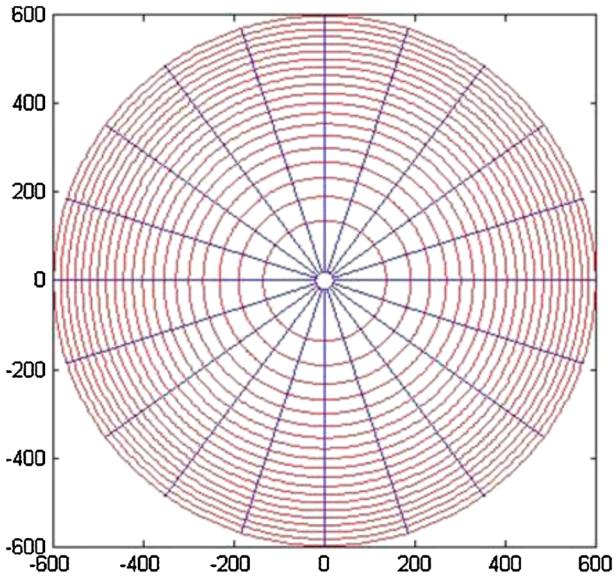

Figure 6. Steady state source flow with stream lines (blue rays) and expansion of extrusion outline (red circles) for regular time steps. This is the projected stream line and velocity profile for a 2-D source emanating onto perfectly horizontal plate.

The radial velocity, u_r, at any distance, r, from the 2-D source origin (assuming h is a constant unit height) is at any one time related to the source flux, Q:

$$Q = h\int_0^{2\pi} u_r r \mathrm{d}\theta \quad \left[\mathrm{m}^3\ \mathrm{s}^{-1}\right] \qquad (2)$$

The tangential velocity is everywhere zero. From equation (2) follows that the radial velocity, u_r, is

$$u_r = Q/2\pi hr \quad \left[\mathrm{m\ s}^{-1}\right] \qquad (3)$$

©2014. American Geophysical Union. All Rights Reserved.

The strength, m, of the source (positive for a source and negative for a sink) can be defined as

$$m = Q/2\pi h \quad \left[\mathrm{m}^2\ \mathrm{s}^{-1}\right] \tag{4}$$

The radial velocity, u_r, can be concisely expressed by

$$u_r = m/r \quad \left[\mathrm{ms}^{-1}\right] \tag{5}$$

The radial velocity profile becomes time dependent when the flux strength Q is unsteady (and thus time dependent itself [$Q(t)$]).

The thin sheet approximation retains some important characteristics of geological gravity flows and is adopted here because it allows for a concise mathematical analysis. This study is restricted to gravity flows of high-viscosity fluids ($Re < 1$) that spread subaerially from a circular orifice onto a planar surface (either perfectly horizontal or sloping). The high-viscosity fluid is incompressible; its viscosity is assumed to remain constant and Newtonian over time. The source flow advances in laminar fashion; inertia remains absent in high-viscosity fluids. An infinite flow space can be adopted as a good approximation of the boundary conditions at all times, because the flow is carried by a high-viscosity fluid displacing air, which has a negligible resistance to flow; hence, the assumption of an infinite 2-D flow continuum is justified. In the potential model approximation, issued fluid propagates with spatially varying but steady rates in an any particular location of the 2-D flow space (r,Θ) when the flux Q is steady from the onset. In the absence of a slope (no far-field flow) the radial velocity profile is given by $u_R = Q/2\pi hr$. The spatial variation of u_r graphed in Figure 6 includes the contours for progressive spreading of the outline of the fluid volume issued from the source, assuming constant Q.

Gravity flows in high-viscosity fluids may occur either in steady state or various modes of transient flow, depending upon the rate and steadiness of the source flux. In the Hele-Shaw approximation above relationships between Q and u_r still hold, even when Q is time dependent. The constant thickness approximation of our model corresponds to curl free and thin flow. The vorticity (curl) is negligible ($\dot{\omega} \approx 0$), because (1) the contribution of the vertical pressure gradient to the lateral velocity field can be neglected and (2) lateral boundaries in the 2-D flow plane are absent. In many natural flows the effects of lateral changes in h on the flow kinematics remain small when the spreading layer evolves as a thin sheet and with lateral thickness variations remaining small compared to the mean thickness and occurring much slower than the relatively rapid changes in the horizontal extent of the flow (see section 2.3). We focus on the plan view development of the gravity flows and show that a 2-D potential flow will closely match the vertically averaged spreading velocity of 3-D gravity flows provided $\alpha \leq 1$. However, differences between the vertical flow profiles in 2-D analytical descriptions and 3-D gravity flows in nature may lead to deviations from the 3-D prototypes being larger or smaller as per α value (see section 2.5).

2.3. Natural Examples

Numerous geological gravity flows over flat surfaces originate from sources issuing creeping masses at unknown fluxes (Q). Figure 7a shows a small puddle of gaseous mud issued from a central vent and spreading by gravity like pancake batter. Figure 7b is a satellite image of the radially spreading Syahoo salt glacier. The two orthogonal cross sections (Figure 7c) show that the topography changes are minimal (except for its southern ramp) and have negligible impact on the spreading of the salt source. The dynamic bulge observed during the flow of this viscous fountain model (Figure 5a) is similar to that seen in the Syahoo salt diapir in Iran (Figure 7c). The cross-sectional shape of the surface bulge is, at any time, a function of the flux strength and the lateral spreading rate, which is retarded by viscous forces. The presence of a central dynamic bulge in the Syahoo salt sheet indicates that it is actively fed by a diapir with a waxing salt flux ($\alpha > 1$ in accordance with *Huppert* [1982a]). Isochrons for edge displacement of a gravity flow with waxing flux are included in the model of Figure 5a. Although the edge displacement rate for gravity flows with $\alpha > 1$ may remain steady (as is the case in Figure 5a), it may even accelerate with r for $\alpha \to \infty$ [*Huppert*, 1982a].

2.4. Downslope Flow Model Assumptions

Next we adapt our model to take into account the effect of basal slope tilt on the morphological evolution of geological source flows. Unconfined salt glaciers (Figure 1) and piedmont ice glaciers (Figure 2) are gravity flows that move downslope as 3-D sheets. Figures 8a and 8b show our model setup for describing 3-D gravity

©2014. American Geophysical Union. All Rights Reserved.

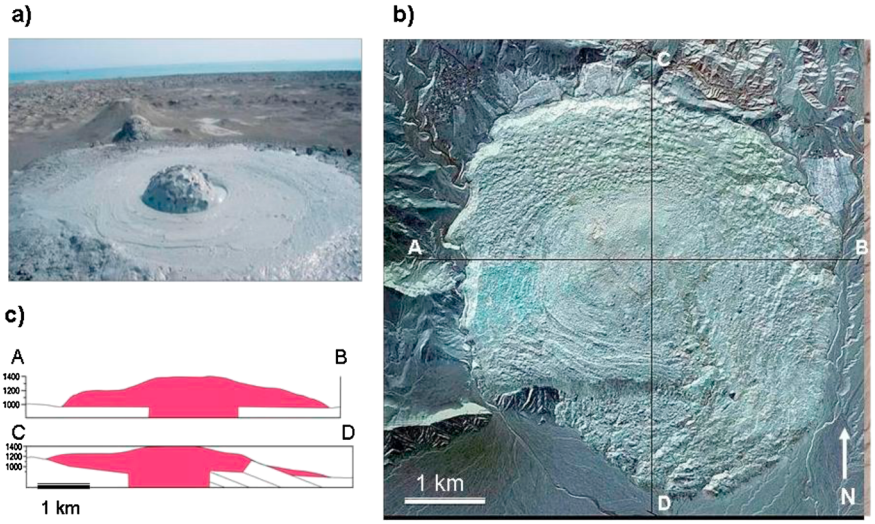

Figure 7. (a) Radial spread of mud from minor vent near Bakhar mud volcano, 57 km SW of Baku, Azerbaijan (Courtesy: Salle Kroonenberg, photo taken 2001). (b) Orthogonal satellite image of Syahoo salt diapir, Iran (27.82°N, 56.25°E) (Courtesy: Google Earth). (c) Geological cross section of salt fountain in Figure 7b showing central bulge, which indicates $\alpha > 1$, and thus, increasing flux strength.

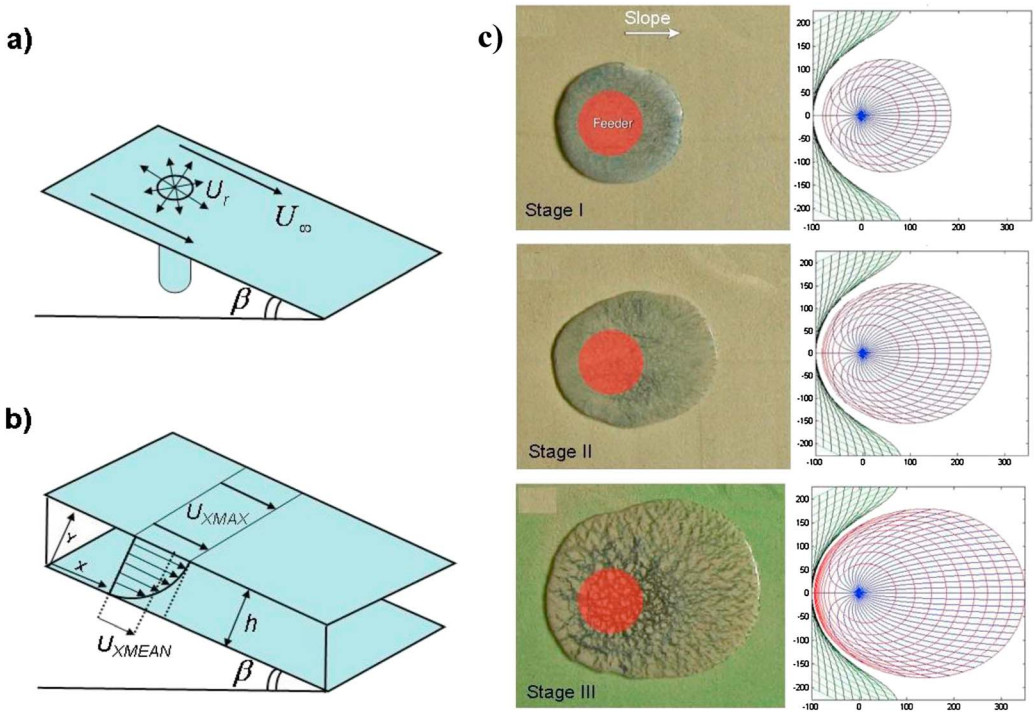

Figure 8. (a) Radial velocity profile of source flow on slope will be perturbed by far-field flow due to slope. (b) Flow of mass on slope can be approximated by channel flow profile; for free-slip, thin layer model, downslope velocity can be approximated by mean velocity. (c) Time series for the planform evolution of a 3-D gravity flow in physical experiment of silicone fluid (viscosity as in Figure 5) issued with a constant flux on a gentle slope (left column). Corresponding analytical 2-D flow approximation (right column) uses virtual superposed far-field flow (green curves for flow lines and black contours for isochrones of flow advancement). The issued source fluid itself has blue curves for flow lines and red contours for fluid displacement isochrons. All time contours are spaced for 20 nondimensional time steps and $Rk = 100$.

©2014. American Geophysical Union. All Rights Reserved.

flows on a slope by a 2-D analysis (not in vertical cross sections but in plan view). The source flux determines the perimeter growth of the mass on the slope (Figure 8a), the angle of which adds the gravitational pull that superposes a downslope velocity on the expelled mass (Figure 8b). The 2-D sheet becomes a proxy model for the 3-D flow by replacing the vertical velocity gradient, which in the real flow displays a Poiseuille flow profile due to a no-slip base (Figure 8b), by a uniform mean velocity $u_{X\mathrm{MEAN}}$ that for channel flow is a function of u_{MAX} in the top of the fluid layer [e.g., *Spurk and Aksel*, 2008]:

$$U_{X\mathrm{MEAN}} = (2/3)u_{X\mathrm{MAX}} \quad \left[\mathrm{ms}^{-1}\right] \tag{6}$$

Even if lateral thickness changes occur in downslope direction, expression (6) is still valid. The principal driving force in downslope direction is the downslope component of gravity; pressure variations due to liquid depth changes are assumed negligible.

A physical laboratory experiment was conducted with silicone fluid issued at constant flux onto a gentle slope to illustrate the evolution of a high-viscosity gravity flow spreading subaerially with steady flux Q (Figures 8c, left column). The planform outlines of the 3-D gravity flow on the planar slope (Stages I–III) are compared to those of a 2-D analytical model, using appropriate similarity scaling parameters (Figures 8c, right column). The perimeters of the 3-D physical gravity flow and 2-D analytical solutions match very closely in all stages of the gravity current advance.

In all our 2-D models we use a scalable but constant mean velocity for the far-field flow. In the physical models (Figure 8c) and in nature (Figures 1 and 2), the far-field velocity vector is determined mainly by the topographical slope and viscosity of the source fluid. More precisely, Poiseuille channel flow due to the pressure gradient induced by the slope will have a mean velocity, $u_{X\mathrm{MEAN}}$, determined by the horizontal velocity u_x in the vertical flow profile:

$$u_{X\mathrm{MEAN}} = \int_0^h \frac{u_x(y)}{h} dy \quad \left[\mathrm{ms}^{-1}\right] \tag{7a}$$

The velocity profile, $u_x(y)$, is for the downslope gravity flow given by [*Spurk and Aksel*, 2008, p. 173]

$$u_x(y) = \frac{\rho g \sin\beta}{2\eta} h^2 \left[2 - \frac{y}{h}\right] \frac{y}{h} = \frac{\rho g \sin\beta}{2\eta} \left(2hy - y^2\right) \quad \left[\mathrm{ms}^{-1}\right] \tag{7b}$$

Parameters in equation (7b) are the layer thickness, h, basal slope angle, β, gravity acceleration, g, fluid density, ρ, and fluid viscosity, η. The maximum velocity, $u_{X\mathrm{MAX}}$, occurs in the top of the fluid layer (where $y = h$) and where equation (7b) simplifies to

$$u_{X\mathrm{MAX}} = \frac{\rho g \sin\beta}{2\eta} h^2 \quad \left[\mathrm{ms}^{-1}\right] \tag{7c}$$

The mean velocity for the parabolic flow profile is $u_{X\mathrm{MEAN}} = 2/3(u_{X\mathrm{MAX}})$ [e.g., *Spurk and Aksel*, 2008]. Thus, the mean of the downslope flow rate is inversely proportional to the viscosity. The sine of the slope angle β varies only within a tight fractional range, but the viscosity may vary over many orders of magnitude, which is why $u_{X\mathrm{MEAN}}$ may also vary over many orders of magnitude for gravity flows ranging from salt to mud. Table 1 summarizes the established viscosity ranges for salt, ice, lava, and mud flows. Gravity flow shapes are also affected by the flux rate history of the flow source. Because natural materials have such a large variation in effective viscosities—generally larger than the other factors (h, β, g, and ρ)—it is clear that gravity flows may evolve with a large variation in planforms and perimeters.

In spite of the large variation in viscosity, the kinematics of subaerial gravity flows of high-viscosity fluids ($Re < 1$) are generally similar and can be approximated by a Rankine flow model (section 3). Scaling of the flow equations reveals that the shape of such gravity flows on subplanar slopes is largely determined by the relative magnitude of the volumetric flux strength of the source and the downslope gravity flow rate, which in turn is determined by the slope angle and viscosity of the mass moving downslope. Using this insight, our study shows how differences in the plume-like planforms of natural gravity flows arise mainly from their different viscosity ranges and whether their supply comes from a pulsed or a steady feeder source. The 2-D gravity flow approximation described here for general application has already been successfully applied to model the evolution of the Chao coulee (Chile), using multiple source vents on a slope [*Weijermars*, 2014].

©2014. American Geophysical Union. All Rights Reserved.

Table 1. Effective Viscosities of Mass Flows

Mass	Pa s	
Mud	10^6–10^{14}	*Kadirov and Mukhtarov* [2004]
Lava		*Spera* [2000]
Rhyolite	10^7–10^{10}	
Dacite	10^5–10^8	
Andesite	10^2–10^5	
Basalt	10–10^2	
Komatiite	10^{-1}–10°	
Salt	10^{15}–10^{19}	*Van Keken et al.* [1993] and *Wagner and Jackson* [2011]
Ice	10^{12}–10^{17}	*Marshall* [2005]

2.5. Limitations of Thin Layer Approximation

A limitation of the 2-D analytical flow description introduced in this study is that lateral thickness changes occurring in natural gravity flows are precluded in the model. To demonstrate what this means for the validity of our 2-D thin layer description of 3-D gravity flows, we first evaluate the nature of thickness changes in 3-D creeping gravity flows for a range of initial conditions.

For flows with constant volume (V, for $\alpha = 0$), transient flow occurs to establish, no matter what the initial shape was, the typical equilibrium shape for a spreading fluid on a *horizontal plane*; duration of the transition depends on the initial shape and height (h_0) of the dead mass (Figure 9a). A gravity current for the constant volume case will maintain an average height $\overline{h}$, which for a 2-D gravity flow with x axis in direction of horizontal flow and perimeter extent x_N, at anyone time is given by

$$\overline{h} = \frac{V}{x_N d} \quad [m] \tag{8a}$$

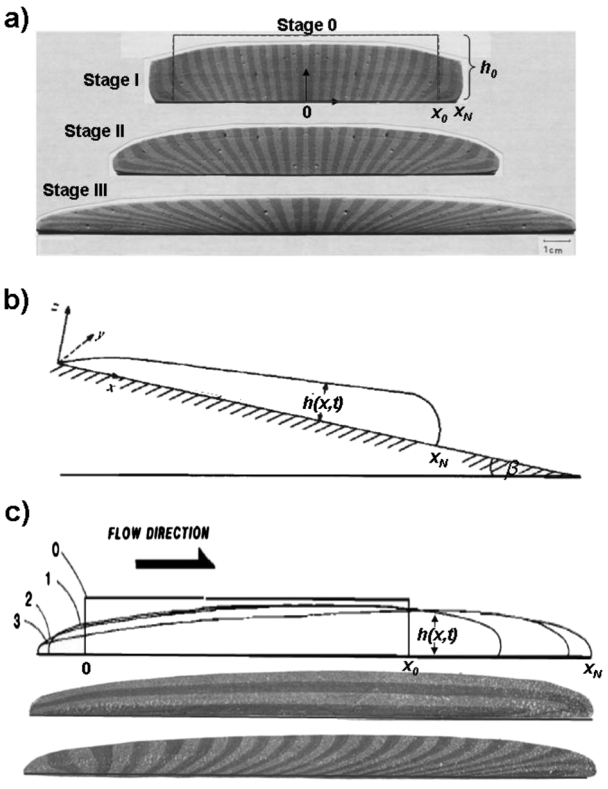

Figure 9. Layer thickness changes during viscous collapse of dead weight masses. (a) Progressive spreading stages (I–III) of high-viscosity silicone (viscosity as in Figures 5 and 8c) with passive dye stripes starting out as a rectangular block (Stage 0). (b) Principle sketch of equilibrium envelope for constant volume flow on a slope. (c) Sketch of silicone fluid spreading on a gentle slope to the right, with final stages of the actual experiment shown in two identical cross sections but dyed with originally horizontal and vertical stripes, respectively. (Sources: (Figure 9a) *Ramberg* [1981], p. 224, (Figure 9b) *Huppert* [1982b], and (Figure 9c) *Brun and Merle* [1985].)

The unit length scale, d, is normal to the plane of view. Height $\overline{h}$ will continue to decline as time passes and as x_N advances laterally outward.

When a dead mass collapses on a *sloping plane* (Figure 9b), the fluid develops a surficial envelope that has been described in detail by *Huppert* [1982b]. Independent experimental data (Figure 9c) (unaware of *Huppert* [1982b] when originally published by *Brun and Merle* [1985]) confirm the theoretical predicted shape development. The average height given in equation (8a) will still apply, but $h(x,t)$ will increase beyond $\overline{h}$ in downslope direction. Although the thickness of h increases near the nose of the current, the actual slope remains extremely shallow in most natural flows (generally much less than 10°). Cases of $\alpha = 0$ (either on horizontal or sloping planar surface) have no active source flux and therefore are not described by our analytical model.

Our study focuses on gravity currents fed by active point sources. For growth or decline of the flux, Q, parameter, α, used in gravity current literature [*Huppert*, 1982a, 2006] provides a measure for the volumetric flux change at any time ($\sim t^{\alpha}$): when $0 < \alpha < 1$, the flux is declining; for $\alpha > 1$, the flux is growing; and for $\alpha = 1$, the flux is constant. In

©2014. American Geophysical Union. All Rights Reserved.

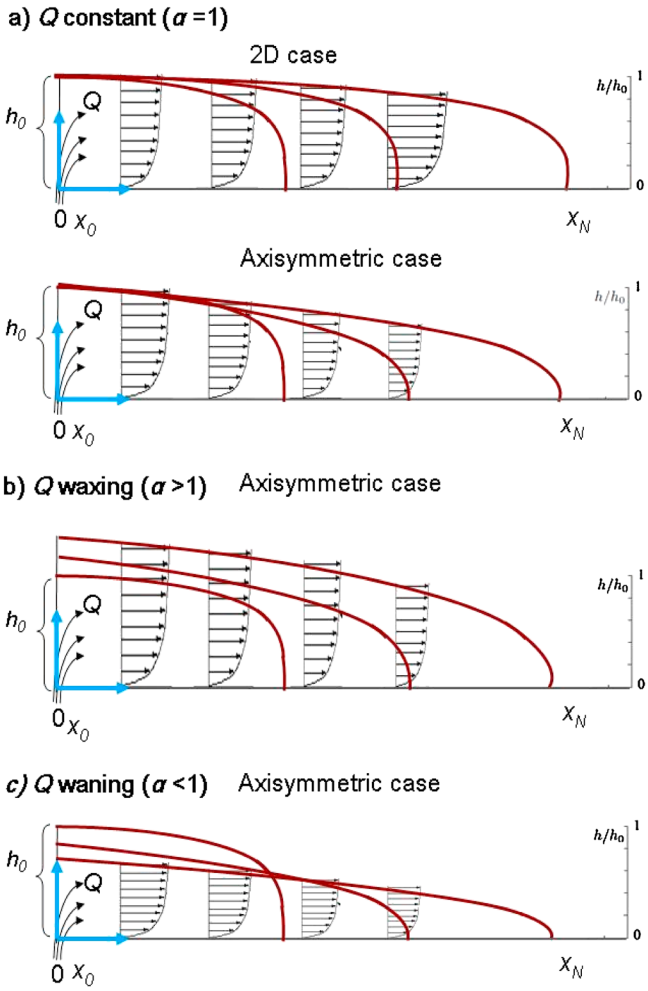

Figure 10. Principle diagrams of gravity flow envelope development (vertical sections) for various initial conditions with active source flux Q.

subaerial gravity flows on a horizontal planar surface, a steady state flow profile (where the gravity flow expands but maintains the same shape) will only occur when the flux, Q, is constant (Figure 4b). For constant flux sources and 2-D gravity flows, an epoch of transient flow occurs to establish the equilibrium height above the source after which a constant thickness h will be retained by the fluid above the source. The average height $\overline{h}$ of the spreading sheet is (Figure 10a)

$$\overline{h} = \frac{Qt}{x_N d} \quad [m] \tag{8b}$$

This expression applies to all 2-D gravity flows with an active source: Q may be constant, waxing, or waning. When Q is constant, $\overline{h}$ will remain constant throughout the spreading history. There is no significant layer thickness change above steady sources, and vertically averaged velocities are time independent (Figure 10a (top)). When Q is waxing, $\overline{h}$ will increase; reversely, when Q is waning, $\overline{h}$ will decline according to expression (8b).

For axisymmetric spreading flows with a point source the average height $\overline{h}$ is (Figure 10a (bottom))

$$\overline{h} = \frac{Qt}{\pi R_N^2} \quad [m] \tag{8c}$$

For constant Q height $\overline{h}$ will decline with $1/R_N$. For waxing Q, height $\overline{h}$ may become constant or even grows as the fluid advances (Figure 10b); for waning Q height $\overline{h}$ will decline (Figure 10c), all according to Q/R_N .

Our 2-D analytical solutions are exact for constant thickness flows (see sections 3–5) but are only qualitatively valid for natural gravity flows with $0 < \alpha \leq 1$, because lateral thickness changes do occur in such 3-D flows. However, the constant layer thickness approximation in our thin layer model is defensible for all cases of mature gravity flows when $0 < \alpha \leq 1$ where layer height rapidly becomes several orders of magnitude smaller than lateral length. Changes in layer thickness remain relatively small as the perimeter of the expanding source flow moves away from the source and the horizontal extent of the spreading fluid becomes rapidly much larger than its vertical thickness. This explains the close match between 3-D physical models and 2-D analytical models of gravity flow with constant flux (e.g., Figure 8c). We argue that our 2-D thin layer approximation still yields reasonable kinematic similarity [*Weijermars and Schmeling*, 1986] for mature 3-D gravity flows when $0 < \alpha \leq 1$, because transient layer thickness changes occur at rates relatively insignificant as compared to the lateral displacement rates. Arguably, many natural flows set on very rapidly, almost with an instantaneous flux start, such as is the case in volcanic eruptions, followed by declining flux rates during the life cycle of the eruption (i.e., $\alpha \leq 1$, as modeled in Figures 20a–20c, see later).

For $\alpha > 1$, the flux rate increases over time and a dynamic bulge grows above the flux source [*Huppert*, 1982a; *Lister*, 1992] due to which the kinematic similarity between natural 3-D gravity flows and the 2-D model

©2014. American Geophysical Union. All Rights Reserved.

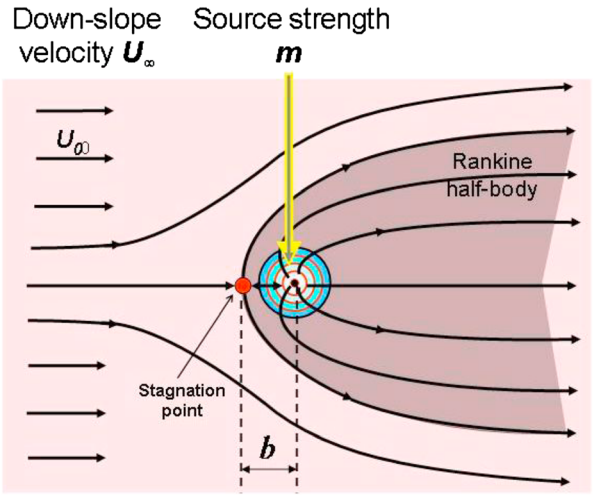

Figure 11. Top view for superposition of source flow and uniform far-field flow results in 2-D Rankine half body. Flow direction between source vent and stagnation point is opposite to overall flow direction. Separation distance "*b*" between source and stagnation point is determined by the relative rates of source flow and far-field flow.

approximation progressively breaks down. Any increase of the flux rate causes storage of fluid in height appreciation. Some natural gravity flows may be fed by an initial waxing flux ($\alpha > 1$) from their feeder stock that later reverses into a waning flux ($\alpha < 1$) due to depletion of the source fluid (and pressure drop in the feeder stock) as can be modeled by bell-shaped flux rate curves (see Appendix D). As noted, for $\alpha > 1$ our thin layer approximation will more rapidly loose kinematic similarity with 3-D gravity flows. In spite of the limitations of our 2-D potential flow approximation, we believe that our quantitative 2-D model results provide important insight for the planform evolution of 3-D gravity flows.

3. Rankine Flow Model

Our models systematically map the theoretical range in shapes evolving by various combinations of source flux strengths and downslope ("far-field") velocity due to gravity. The flow visualizations are based on 2-D mathematical descriptions of source flows (Appendix B). The visualizations are valid for incompressible (vanishing divergence) and irrotational flows (vanishing curl), meaning free slip is assumed at any physical boundaries. Our simplifying assumptions provide valid results for the overall approximation of the flow dynamics in a monitoring layer that is sufficiently far away from boundary layer effects. The uniform flow rate downslope always becomes more dominant farther from the source, hence the steep curvature of the instantaneous flow paths near the source (Figure 11).

The dimensional velocity field around source flows perturbed by a superposed uniform far-field flow (Figure 11) follows from equations introduced by Rankine [cf. *White*, 2011]. Although the final set of equations is found in basic textbooks [cf. *White*, 2011], we think that it is useful to demonstrate in a rigorous approach how these specific solutions relate to the Navier-Stokes equation for a viscous fluid in motion (Appendices A and B). The final set of equations (equations (B16a) and (B16b)) then provides a robust starting point for our subsequent analysis:

$$u_x = U_\infty + (m/r)\cos\theta \quad \left[\mathrm{ms}^{-1}\right] \tag{9a}$$

$$u_y = (m/r)\sin\theta \quad \left[\mathrm{ms}^{-1}\right] \tag{9b}$$

The nondimensional velocities (ux^*, uy^*) in the gravity flow field are given by

$$u_x^* = u_x/U_\infty = 1 + (b^*/r^*)\cos\theta \tag{10a}$$

$$u_y^* = u_y/U_\infty = (b^*/r^*)\sin\theta \tag{10b}$$

The scaling parameters are $b^* = b/r_0$, $r^* = r/r_0$, and $b = m/U_\infty$, and r_0 is a characteristic length scale. The Rankine number (*Rk*) introduced here is defined as

$$Rk = b^* = m/(U_\infty r_0) \tag{11a}$$

For any chosen length unit r_0, the nondimensional number *Rk* uniquely determines the flow pattern due to a source flow with strength *m* with a superposed uniform far-field flow U_∞. When we have a constant source strength, constant fluid viscosity and constant slope, the shape of the streamlines can be characterized by the *Rk* value (Figure 12):

$$Rk = b^* = m/(u_{X\mathrm{MEAN}}\, r_0) \tag{11b}$$

©2014. American Geophysical Union. All Rights Reserved.

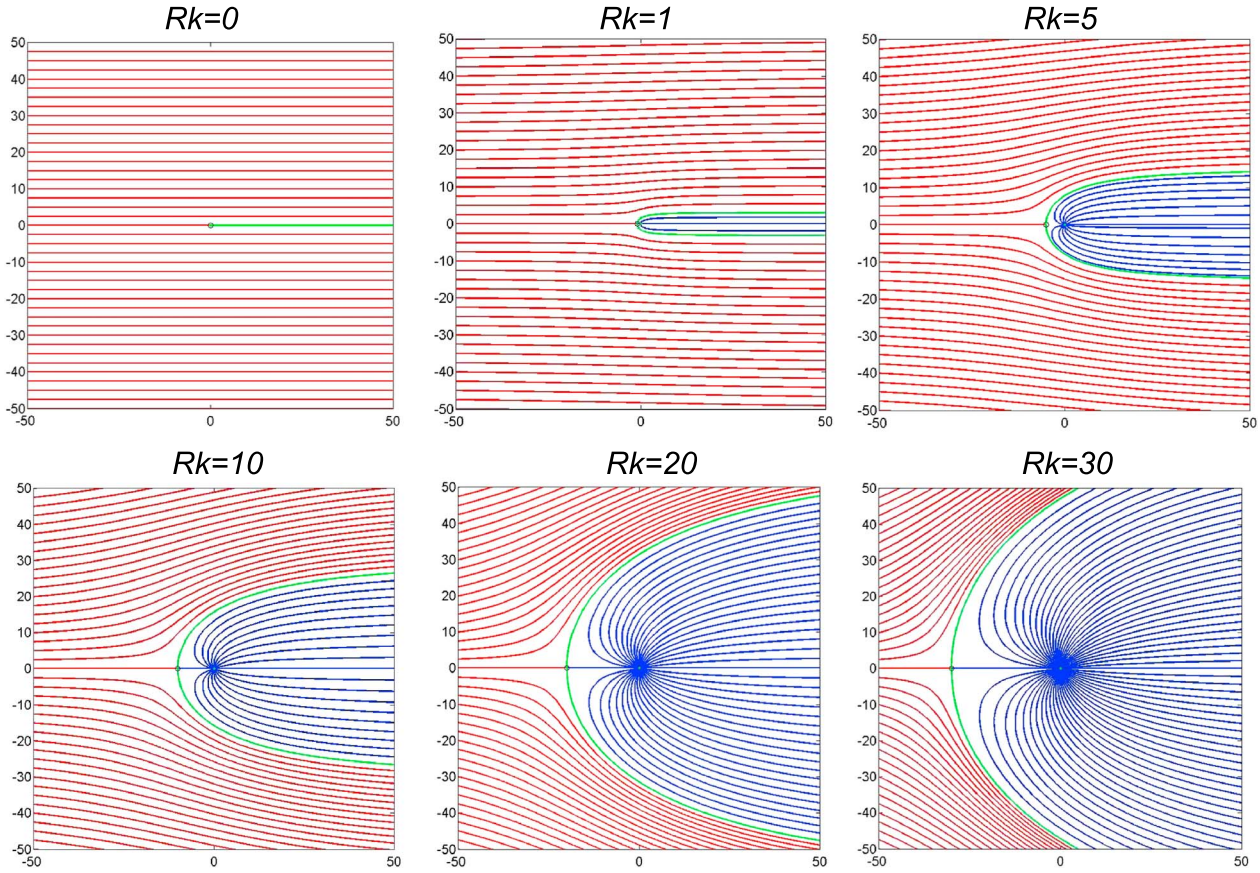

Figure 12. Visualizations of flow lines of uniform far-field flow (red curves) superposed on source flow (blue curves). Fluid particle paths from far-field flow and source flow do not cross and are separated by green curve through stagnation point. Nondimensional field of view, scaled relative to unit length = 100 by 100. All *Rk* numbers are upscaled by factor $2\pi/5$ for practical convenience. MATLAB models generated from our analytical flow equations.

The streamlines can be traced by letting particles at an initial position (r^*, θ) travel according to the velocity field of equations ((10a) and (10b)) using nondimensional time steps given by

$$t^* = (t\, U_\infty)/\, b \tag{12}$$

The flow lines of Figure 12 are valid for steady state *Rk* numbers (positive *Rk* indicates a source flow and negative *Rk* designate a sink flow). Flow lines have been evaluated as discrete particle path solutions using MATLAB. The stagnation point is located at $(x,y) = (-b,0)$. We also varied the b values, implied in the *Rk* number, using various mathematical functions, resulting in time-dependent particle paths as illustrated in Figures 13a–13c.

4. Basic Model Results

We used the functions that control *Rk* to map the range of possible plume shapes for source flows on a slope. The (virtual) downslope far-field flow component is separately visualized and will occur as straight downslope lines (Figure 14) that remain unperturbed when no source is activated. When a source is active, we distinguish between steady sources (section 4.1) and nonsteady sources (section 4.2).

Each set of equations for our models is simple, but varying the key parameters creates huge variations in morphology. This is illustrated below, using a MATLAB code to plot the shapes of the deforming source flows based on the nondimensional Rankine flow equations developed in the previous section. The visualized rates and shapes help to understand how variations in finite plume shapes in natural gravity flows reveal something about their geophysical flow conditions.

©2014. American Geophysical Union. All Rights Reserved.

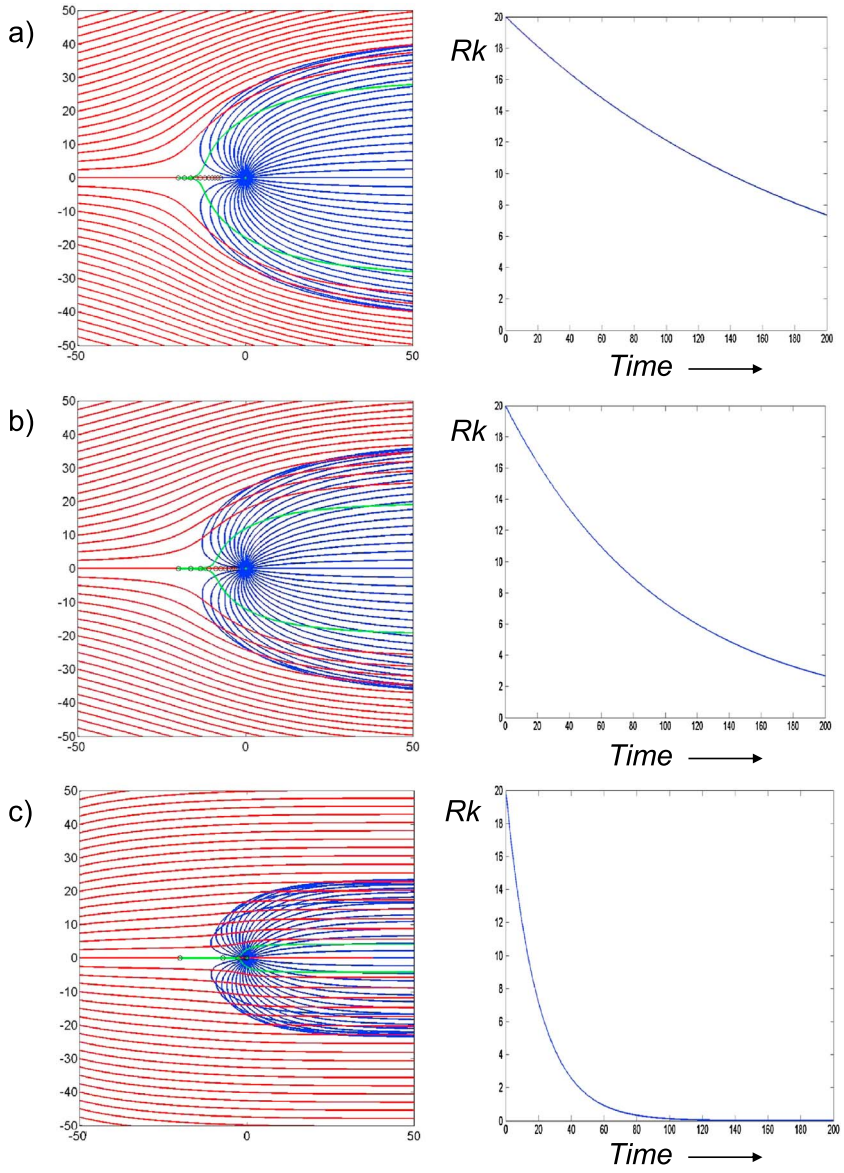

Figure 13. (a–c) Visualizations of particle paths due to superposition of a uniform far-field flow (red curves) and source flows (blue curves) with various time-dependent *Rk* values. Fluid particle paths from far-field flow and source flow cross as stagnation point moves toward the center of source flow. Only a final region outlined by green particle path separates (1) particle paths originating from source (blue curves) that were never crossed by (2) particle paths from far-field flow (red curves). Nondimensional field of view, scaled relative to unit length, is 100 by 100. On right-hand side, corresponding decline curves start at $Rk = 20$ and decline according to a decline function with rates −0.005, −0.01, and −0.05 over 200 nondimensional time steps (horizontal scales). MATLAB models generated from our analytical flow equations.

4.1. Steady Source Flows ($\alpha = 1$; Constant *Rk*)

When source flows with constant source strength are skewed by a constant far-field flow, one can consider different cases, for the relative strength of the source and the far-field flow to control *Rk* and map the full range of possible plume shapes. Figure 15 illustrates how source flow geometry evolves for a range of positive constant *Rk* values. Each plot in Figure 15 shows the same time increments (200 units of nondimensional time) in all six graphs. Far-field flow lines are green, and source flow lines are blue. Black contours are timelines in the far-field flow. Far-field flow lines (green) show the advance of fluid particles during the same nondimensional time as for the source flow contours (red). Red contours outline the shape change (during 20 nondimensional time steps) of an initially circular fluid body (at $t^* = 0$) extruding from the

©2014. American Geophysical Union. All Rights Reserved.

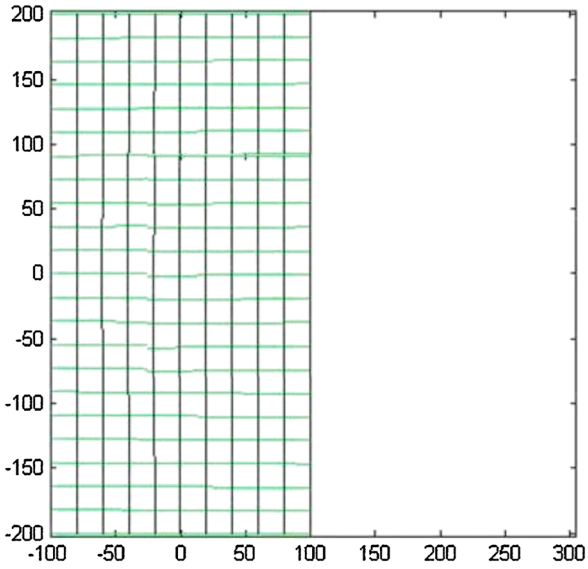

Figure 14. Steady state uniform far-field flow of thin fluid film on planar surface with uniform slope toward the right with particle paths (green lines) and displacement marker contours (black lines) for regular time steps.

source. The green flow lines and black contours visualize the slope velocity, but they are also valid for a horizontal planar surface where a source flow is engulfed by a far-field fluid having the same viscosity as the source flow.

The plots in Figure 15 are based on the Rankine flow equations. The relative strength of source flow and far-field flow are both constant for a given *Rk* (labeled in Figure 15 by *Rk* value on top of each graph). For example, $Rk = 1$ means that the strength of the source flow matches the far-field flow rate down the slope. Assuming a constant slope, when *Rk* increases, the source flow strengthens relative to the superposed uniform flow. When an extrusion becomes faster relative to the constant far-field flow, the plume shape of the source flow predictably broadens.

Figure 16 shows a natural example of a volcanic mud flow, which is narrow and long, suggesting that *Rk* is low. The hyperbolic flow profile of this gravity flow with laterally free boundaries is mirrored in the wrinkles resulting from folding of the mud's cooling, drying surface skin. Similar structures are well known in pahoehoe lava flows having a cooling skin. The maximum width *W* of a Rankine body far downstream is given by $2\pi m/U_{\infty}$, which means $m = 2\pi W U_{\infty}$ [$m^2\,s^{-1}$]. Observing the flow rate U_{∞} in a flow of known width thus can provide estimates for the source strength *m*. For the 60 cm wide mud flow of Figure 16 and observed maximum flow rates of $U_{\infty} = 4\,mm\,s^{-1}$ [*Hovland et al.*, 1997], the corresponding peak extrusion flux will be $m = 0.015\,m^2\,s^{-1}$ or $0.9\,m^2\,min^{-1}$.

Figure 17 outlines plume shapes for very large *Rk* values. Conditions are similar to those in Figure 15 but the field of view is zoomed out to encompass the plume outline. When the *Rk* value approaches infinity (modeled in Figure 17 by $Rk = 2000$), the source flow becomes increasingly axisymmetric (resembling the single unperturbed source flow of Figure 6); the effect of the downslope flow becomes negligible. Note that the "imaginary" far-field flow representing the superposed flow due to the slope senses the source even before "hitting" it, because both flows are part of a viscous continuum.

4.2. Nonsteady Source Flows ($0 < \alpha < 1$; Declining *Rk*)

Most source flows in nature are unlikely to flow steadily over long timescales. For example, glaciers vary greatly in their volumetric flux. From our survey of high-viscosity geological flows we conclude that declining flux strengths are the most common type in nature. We therefore first modeled source flows with $0 < \alpha < 1$, using various decline functions. The examples of Figures 18a and 18b show the shape evolution of two separate gravity flows, each with declining source flow strengths. The source in Figure 18b declined 10 times faster than the flow in Figure 18a. The time series show how their respective plumes develop into final shapes we coined as racket- and teardrop-shaped plumes.

Such shapes are frequently encountered in natural mud flows. Volcanic mud can have a wide range of viscosities (Table 1), so gravity flows from mud vents can develop into tadpole and teardrop shapes (lower viscosity mud, Figures 19a and 19b), racket shapes (intermediate-viscosity mud, Figure 19c), and pear shapes (higher-viscosity mud, Figure 19d). Although variations in the overall slope may cause fractional changes in the initial *Rk* number, viscosity is the more important factor because it may vary over several orders of magnitude (Table 1) and therefore it impacts the downslope velocity more than does a change in slope (see equation (7c)). The plume shapes are affected by radial fanning, once a gravity flow reaches a subhorizontal surface.

Flow eruption dynamics of mud volcanoes is briefly outlined below to explain why their source strength can decline steeply after an initial, almost instantaneous pulse of flux. About 2000 major mud volcanoes have

©2014. American Geophysical Union. All Rights Reserved.

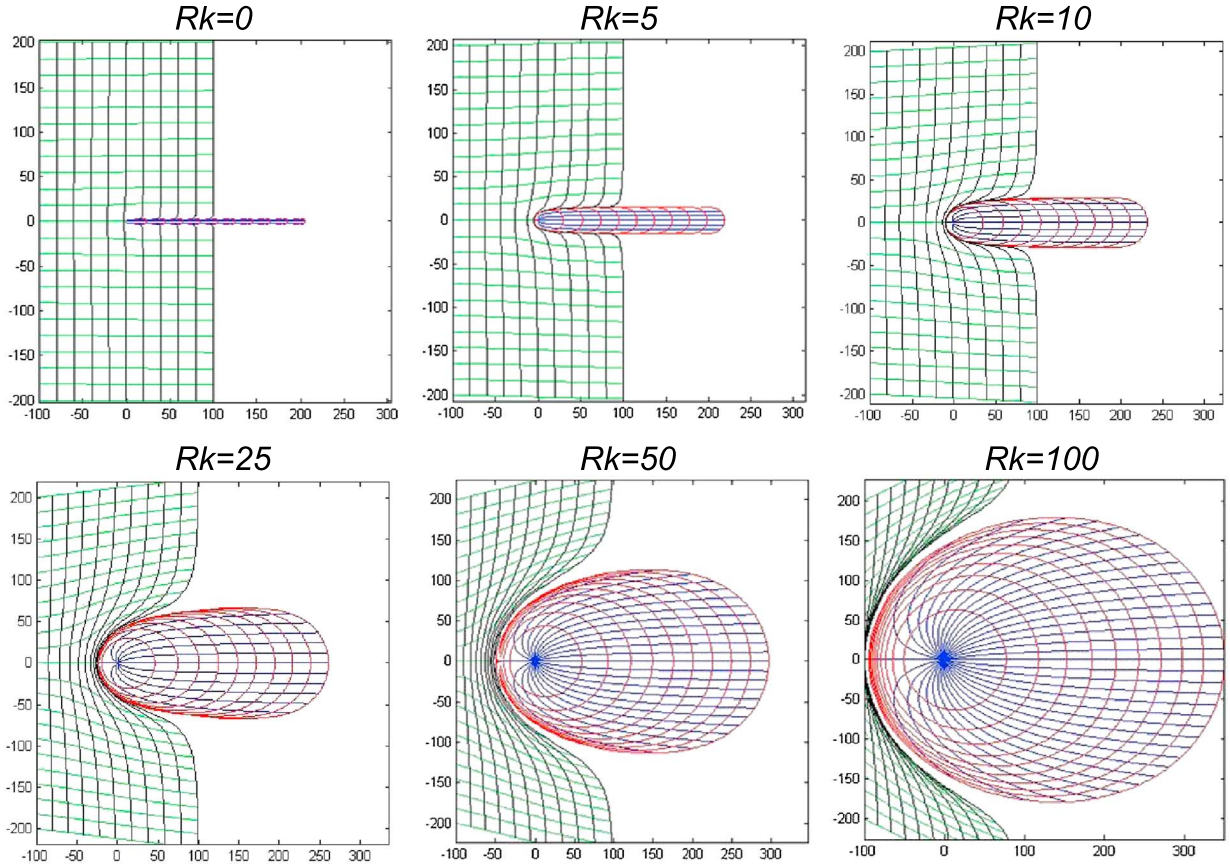

Figure 15. Final planforms of steady state flows with time contours for far-field flow (green curves for flow lines, black contours for time steps) and for source flow (blue curves for flow lines, red contours for time steps). Time contours are spaced for 20 nondimensional time steps. Total run time $t^* = 200$ nondimensional time steps. Different plume shapes due to various (but constant) *Rk* values. Nondimensional field of view, scaled relative to *b* unit length, is 450 by 450. Flow line spacing of source flows reduced for lower *Rk* to avoid clustering of lines. MATLAB models generated from our analytical flow equations.

Figure 16. Mud flow near the Dashgil mud volcano 57 km SW of Baku, Azerbaijan. Total width of the flow is approximately 60 cm. Stream is marked by manually dropped mud flakes to measure flow displacement. Photo was taken in 2001 (courtesy Salle Kroonenberg).

been identified worldwide, both onshore and offshore [*Dimitrov*, 2002]. Many of these mud volcanoes are particularly large, up to 400 m high, and they erupt regularly and episodically. In Azerbaijan, mud volcanism is associated with onshore and offshore hydrocarbon seepage. Approximately 220 onshore mud volcanoes have been reported near Baku, within an area of about 16,000 km^2 [*Guliyev and Feizullayev*, 1997]. The Bakhar mud volcano, located 57 km SW of Baku, has seen eight strong eruptions since 1823. Bordag-Kobi, located 20 km NW of Baku, erupted in 1827, 1894, 1902, 1953, and 1957 [*Scholte*, 2005]. Numerous gryphons, small mounds built by eruptions of mud, occur as small satellites near these major mud volcanoes. The temperature

©2014. American Geophysical Union. All Rights Reserved.

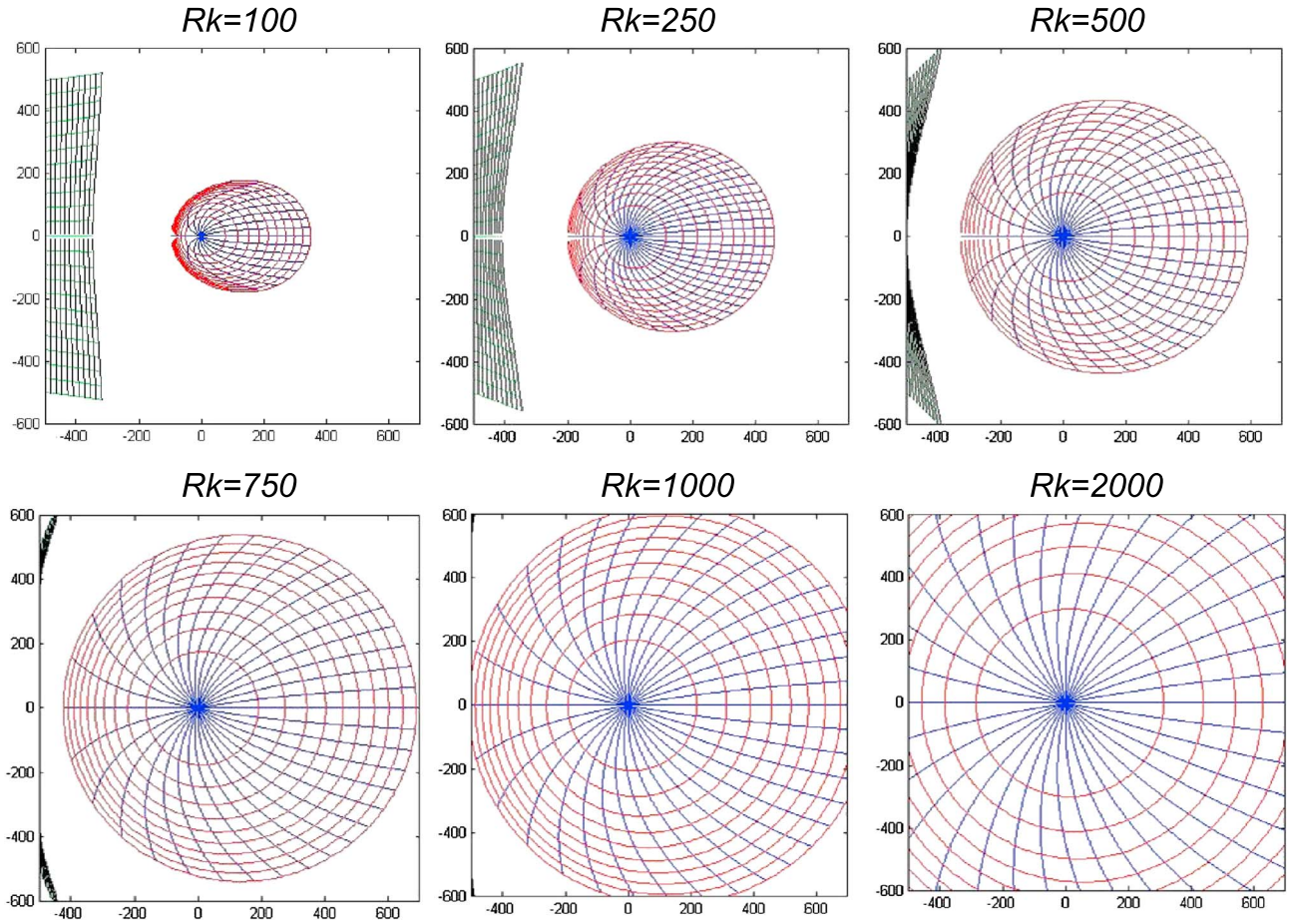

Figure 17. Final planforms for increased strength of source flow (but steady state for each case) resulting in faster sheet spreading and reduction of the relative impact of superposed far-field flow. Time contours are spaced for 20 nondimensional time steps. Total run time t^* is 200 nondimensional time steps. Nondimensional field of view, scaled relative to b unit length, is 100 by 1200. (top) A zoomed-out version of Figure 14, with far-field flow starting farther from the source. For $Rk = \infty$ the flow resembles that in Figure 6, and only perfect circular shapes will occur for source flows with superposed far-field flow that is negligible (as implied by $Rk = \infty$). MATLAB models generated from our analytical flow equations.

of the expelled mud is approximately 21–23°C. The feeder conduits can be as deep as 12 km. Major factors causing episodic mud volcanism in Azerbaijan are tectonic overpressure, density inversion, sediment loading, and gas hydrate dissociation [*Guliyev and Feizullayev*, 1997; *De Lange and Brumsack*, 1998; *Lerche and Bagirov*, 1998; *Milkov*, 2000; *Aloisi et al*., 2000a, 2000b; *Kopf*, 2002]. Mud volcanoes are also reported from the Salton Sea geothermal system (California), where gryphons are exposed in the onshore Davis-Schrimpf seep field [*Svensen et al*., 2007, 2009]. The composition of volcanic mud is highly variable but usually corresponds directly to the nature of the conduit, the presence of hydrocarbons, and the lithology of the mobilized sediments or parent rocks [*Kopf*, 2002]. Our conclusion is that mud eruptions are relatively short lived, which will be reflected in their shapes as typical for erupted mass flows with rapid source strength decline.

The eruption mechanism of mud volcanoes suggests that they start with a certain flux rate ($\alpha = 1$) which immediately decays, effectively varying α between 1 and 0 over the life cycle of the eruption. We mapped out a full set of runs with instantaneous onset of a specific source flux rate followed by source rate decline using a range of decline functions. Several hundred runs were completed to map out a full range of possible shapes. The final plume shapes of source flows on a slope (after 600 nondimensional run time) in Figures 20a–20c were selected as a systematic summary of with representative cases from our simulation runs. The range of finite plume shapes is typical of time-dependent Rk numbers, with $Rk(t)$ declining exponentially as plotted in the bottom row of Figures 20a–20c. To facilitate comparison of the model results with natural flows, we introduce qualitative terms for the range in plume shapes observed (pendulum, teardrop, tadpole, racket,

©2014. American Geophysical Union. All Rights Reserved.

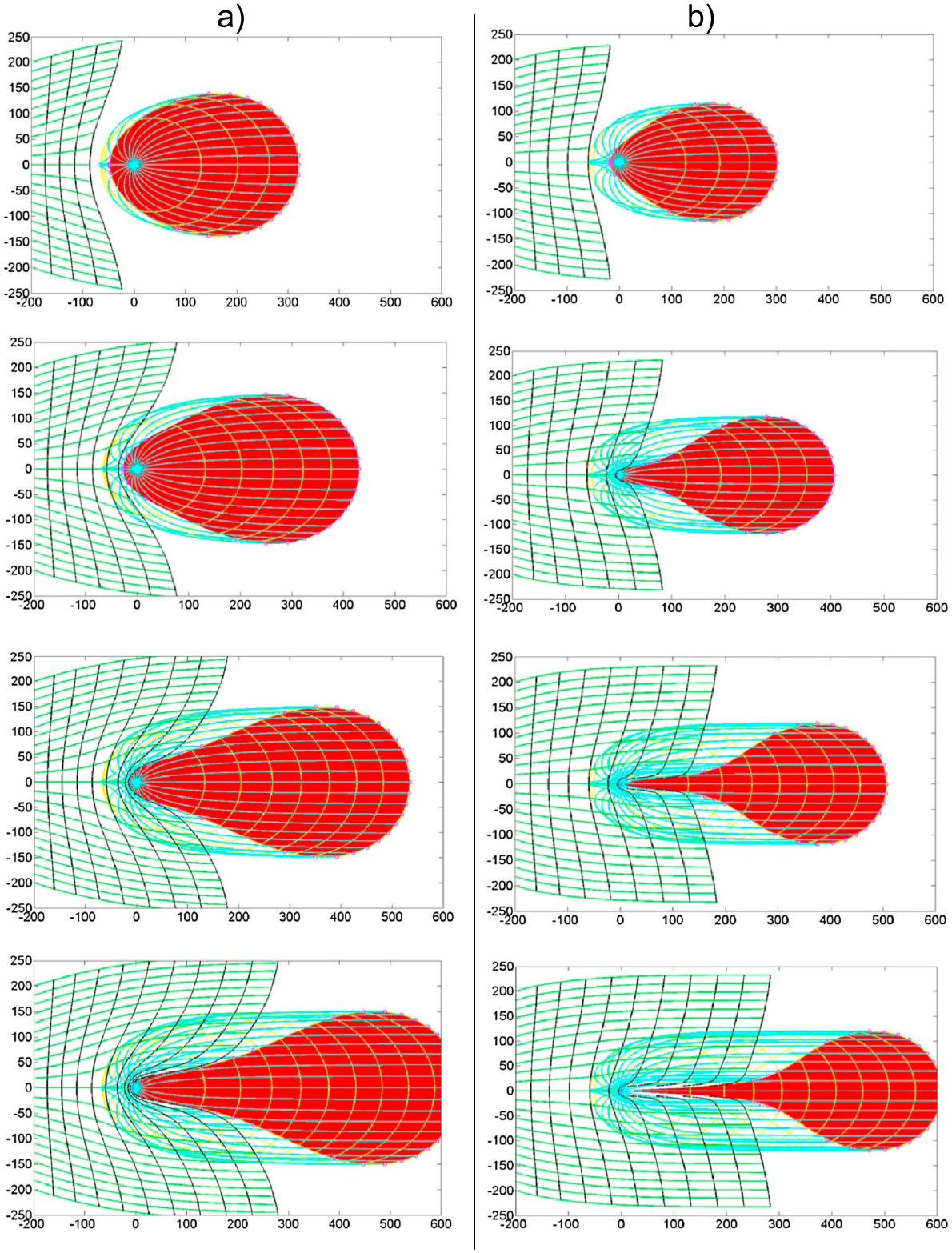

Figure 18. Time series for evolution of plume shapes for time-dependent decline of source flow rate (time-dependent *b* values). (a) Racket-shaped plume growth for initial *Rk* value of 100 and decline rate of −0.005. (b) Teardrop-shaped plume growth for initial *Rk* value of 100 and faster decline rate of −0.01. Run times from top to bottom rows: $t^* = 200$, 300, 400, and 500 nondimensional time units. Corresponding decline curves are included in the summary of Figure 20. Time contours spaced for 50 nondimensional time-lapse intervals. Nondimensional field of view is 800 by 500. Flow line spacing of source flows reduced for lower *Rk* numbers to avoid clustering of lines. MATLAB models generated from our analytical flow equations.

©2014. American Geophysical Union. All Rights Reserved.

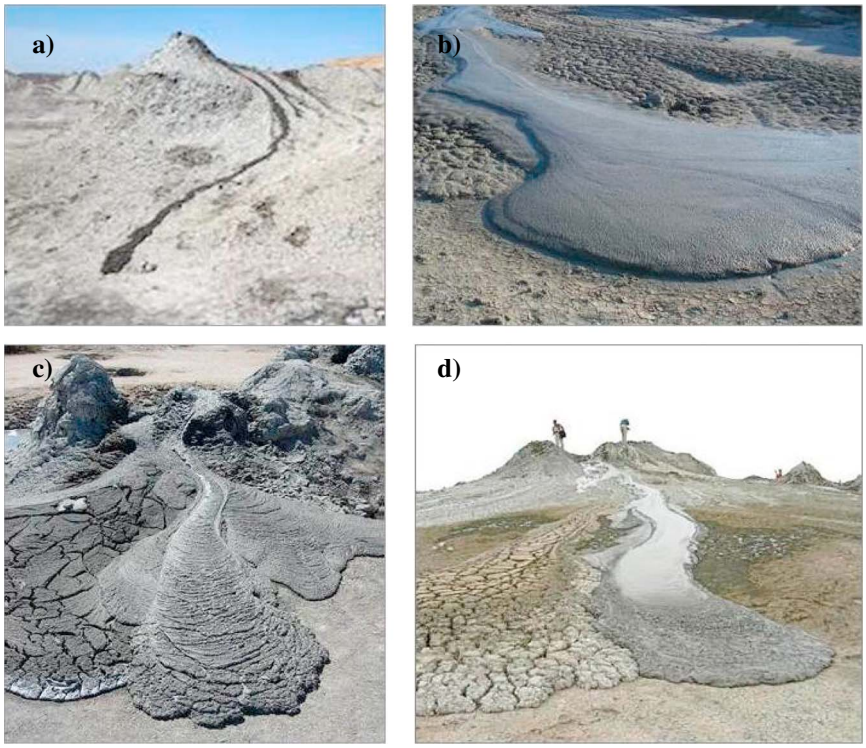

Figure 19. (a) Tadpole-shaped mud flow from gryphon near Gobustan mud volcano, Azerbaijan (courtesy Steve Lioy). (b) Teardrop-shaped mud flow at Gobustan volcano, Azerbaijan (courtesy I.S. Guliyev). (c) Racket-shaped mud flow from gryphon in Davis-Schrimpf mud seep field, California (courtesy Andrew Alden). (d) Similar racket-shaped mud flows at Lokbatan, Azerbaijan.

carrot, club, pear, cigar, torpedo, and eggplant, as annotated in Figures 20a–20c). For all these plume shapes, their narrower ends point upstream.

We also modeled source flows with waxing strengths ($\alpha > 1$; see Appendix C), and these resulted in egg-shaped plumes with the narrower end pointing downstream, which is a conclusive criterion for distinguishing gravity flows formed by waning and waxing source strengths. Although for $\alpha > 1$ our 2-D model will suffer from progressive loss of similarity with 3-D gravity flows in nature (see section 2.5); the general diagnostic criterion formulated here is assumed to apply to 3-D cases.

5. Advanced Model Results (Oscillating α and *Rk*)

5.1. Planform Symmetry and Changes in Width of Lava Flows

Figure 21 shows an 8 km long andesitic lava flow stretching down the Andean Altiplano slope to the WSW from a source at La Poruña scoria cone in the upper left corner of the image. Because of the dominant eastward winds, air fall tephra erupted from the scoria cone fell largely to the east of the vent, while the andesite lava flowed westard. La Poruña scoria cone has a basal diameter of 900 m and is 180 m high. A prominent bocca on the west flank of the cone is the source of the 8 km long compound lava flow. Isolated eruption centers are scattered all over the central Andes (Chile) above dilational zones of regional faults. East of La Poruña cone is the major San Pedro volcano, of which the La Poruña cone may be a satellite vent [*O'Callaghan and Francis*, 1986; *Wörner et al*., 1988]. The viscosity of andesitic lavas having typical extrusion temperatures between 900° and 1300°C ranges between 10^3 and 10^5 Pa s [*Spera*, 2000]. The width of the Poruña lava field varies as it moves down the plane and can only in part be explained by local topography. Small lobes form where topography is locally depressed, but the central section of the Poruña lava sheet is narrow. Variations of wider and narrower sections are mirror imaged about the length axis of the lava flow, which do not correlate with any undulations in topography. We modeled the shapes resulting from cyclic variations or pulsations in source strength during

©2014. American Geophysical Union. All Rights Reserved.

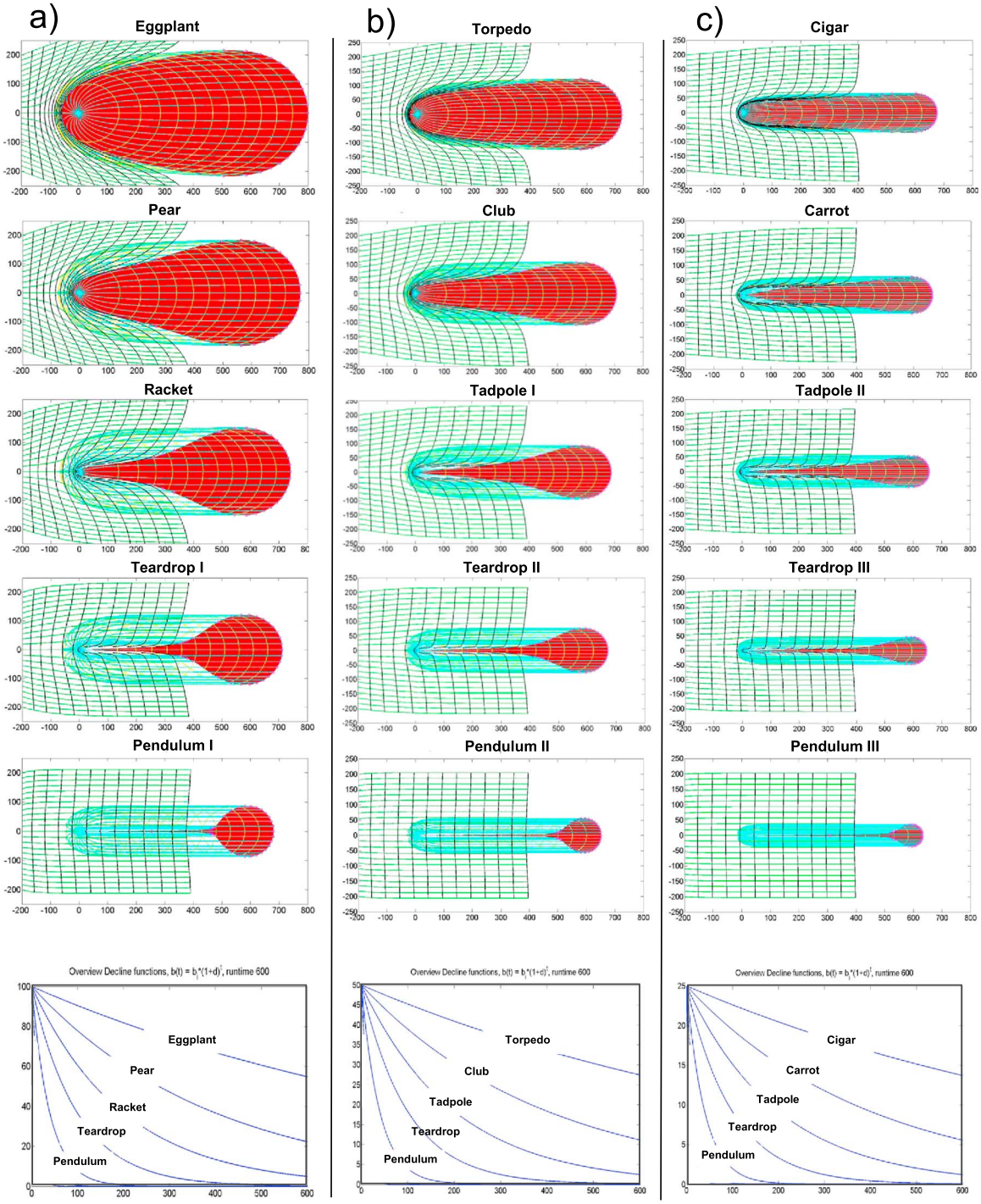

Figure 20. Comprehensive overview of different final plume shapes as source flow ebbs (time-dependent *Rk* values). Time contours spaced for 50 nondimensional time steps. Total run time 600 nondimensional time steps. Nondimensional field of view, scaled relative to unit length, is 1000 by 500. Flow line spacing of source flows reduced for lower *Rk* numbers to avoid clustering of lines. (a) Left-hand column for initial *Rk* values of 100. (b) Middle column for initial *Rk* values of 50. (c) Right-hand column for initial *Rk* values of 25. Top row for slowest decline rate of source flows, second row from the bottom for fastest decline rate of source flow. Corresponding decline rates are shown in the bottom row. MATLAB models generated from our analytical flow equations.

©2014. American Geophysical Union. All Rights Reserved.

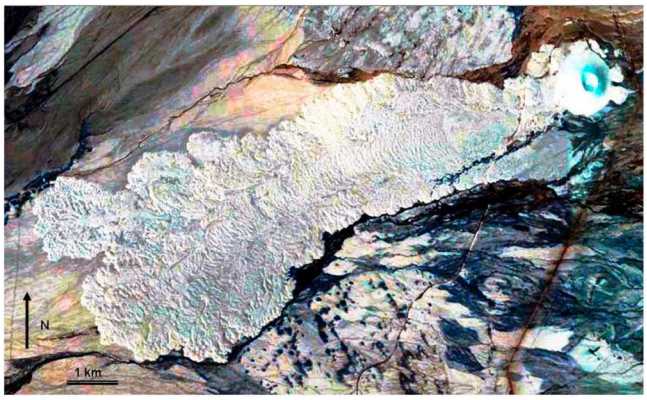

Figure 21. La Poruña andesite flow, from vent at SW base of a cinder cone that is a satellite vent to the Volcan San Pedro. False color thematic mapper image ID = 50378-14014, scene 23377, May 1985 (21°53′33″S, 68°29′55″W).

the eruption (section 5.2), which can explain the changes in width of a volcanic lava sheet like the Poruña lava field as it travels along its axis.

5.2. Models for Periodic Eruption Pulses of Lava Flows

If a source flow oscillates in strength, complex plume shapes may evolve. For example, peanut-shaped plumes develop when the source flow waxes and wanes (Figure 22). These oscillating source strengths could conceivably result from pulses of magma squeezing up a volcanic vent. Figures 22a–22f show a time series; the stage of Figure 22e resembles the shape of the La Poruña lava field of Figure 21, suggesting that three briefly spaced eruptive pulses were responsible for its emplacement. Our conclusion is that lava fields can attain various shapes even when erupting onto a relatively planar slope. The plume shape depends on the spacing and intensity of the magma pulses.

Figures 23a–23f model the effect on the final plume shapes for a range of magmatic pulse rates, which can explain the wide range of lava field shapes that may occur in nature. When plume width perpendicular to its downstream symmetry axis varies greatly, this means that the eruption pulses varied similarly in strength. When the plume width is nearly pinched (Figure 23f), eruption strength paused longer before resuming fuller strength again. Figure 23f is a shape typically observed in pillow lavas, where pulses of expulsion from each pillow are widely spaced in time.

The example of a pillow lava field (Figure 24a) shows that flow in the basal part of two extruding lava pillows is influenced by preexisting minitopography and diverts around a preexisting ridge. The upper lava layers may flow over the basal layers so that the overall lava plume shape is still controlled by the flux strength of its vent source relative to the superposed downslope speed. In spite of the undulations in basal topography, the examples of lava flows in Figures 24a–24c all suggest that major eruption pulses are responsible for their formation. The frontal part of their principal flows is broader, form which their source strengths can be concluded to all have waned after the initial eruption pulse. In conclusion, lava flows, with their enormous range of compositional and temperature-sensitive viscosities [see *Spera*, 2000], may exhibit the full range of gravity flow geometries modeled in Figures 20, 22, and 23.

6. Discussion

The gravity spreading of terrestrial source flows reshapes our planetary surface in both endogenic mass cycles (plate tectonics and magmatism) and exogenic mass cycles (meteoritic impacts, weathering, and erosion). A variety of geological materials is emplaced in high places by active geological forces after which passive gravity forces eventually may pull these masses down a topographical slope once again. Major examples of viscous or viscoplastic gravity flows of terrestrial surface materials from point sources include the noncrystalline flow of lava and mud from volcanic vents and the crystalline creep of salt and ice in glaciers. The wide range of gravity flow shapes encountered in nature can be simulated by our models (but with limitations for $\alpha > 1$).

Ice glaciers and salt glaciers are composed of crystalline rocks having viscosities higher than those of lava flows and higher than most mud flows (Table 1). The flows in the piedmont part of such glaciers with free lateral space fit our Rankine model; the ice streams confined in the upstream valleys act as feeders for the source flow. Elephant Foot Glacier (Greenland) provides a pristine example of a pear-shaped plume formed by issuance of glacier ice onto a piedmont plane (Figure 2a). The shapes of relatively unconstrained terminal tongues of ice glaciers on Axel Heiberg Island provide additional piedmont glacier examples that are predominantly club and torpedo shaped (Figure 2b). Such shapes are typical for gravity flows with large *Rk*

©2014. American Geophysical Union. All Rights Reserved.

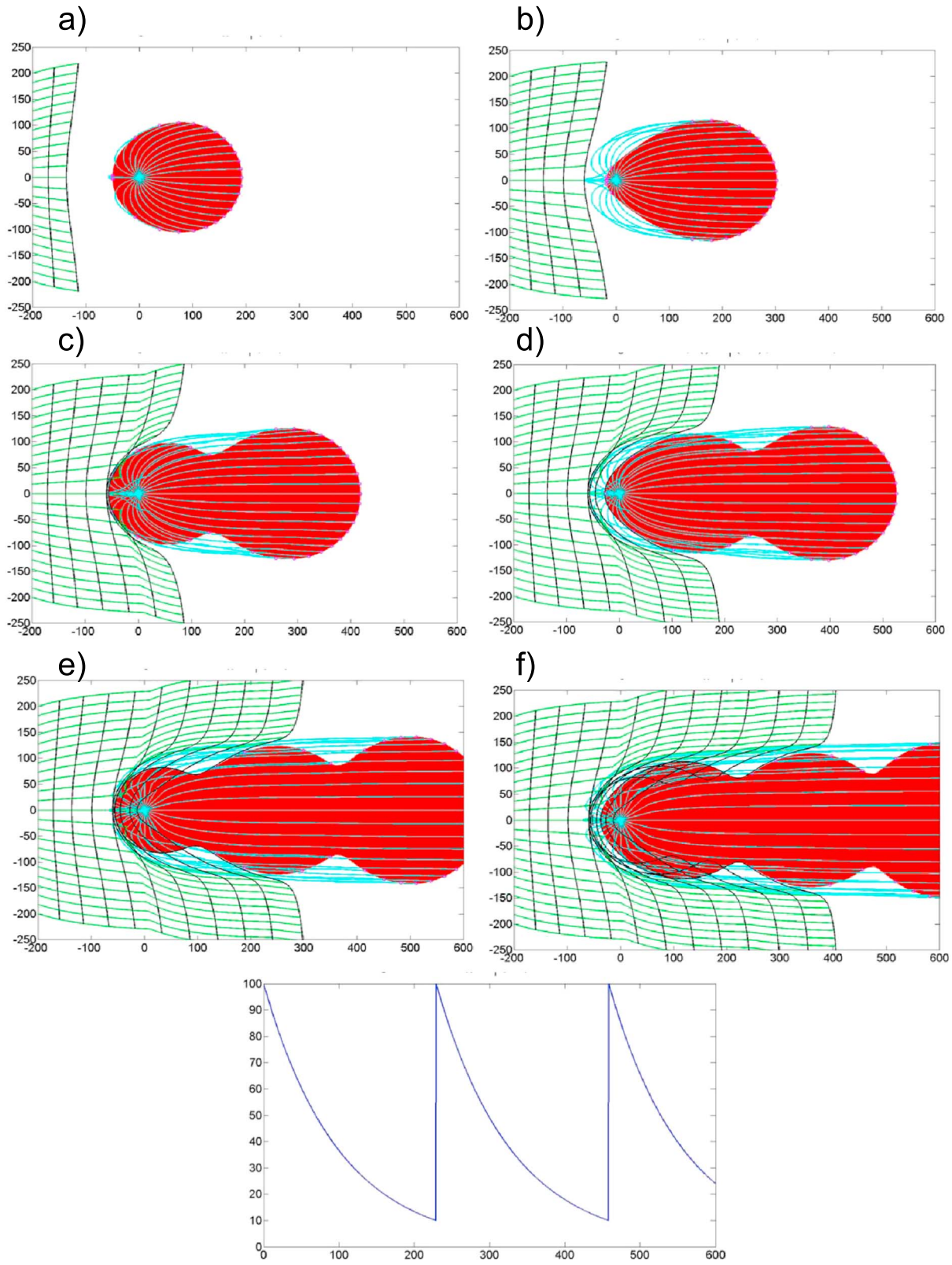

Figure 22. (a–f) Time series for the evolution of source flow plumes due to oscillating strengths of source (time-dependent *Rk* values as shown in the bottom graph). Peanut-shaped plume evolves after increasing time steps. Top to lower rows: $t^* = 100$, 200, 300, 400, 500, and 600 nondimensional time units. Time contours in peanut and downslope gravity flow spaced for 50 nondimensional time steps. Nondimensional field of view, scaled relative to unit length is 800 by 500. MATLAB models generated from our analytical flow equations.

©2014. American Geophysical Union. All Rights Reserved.

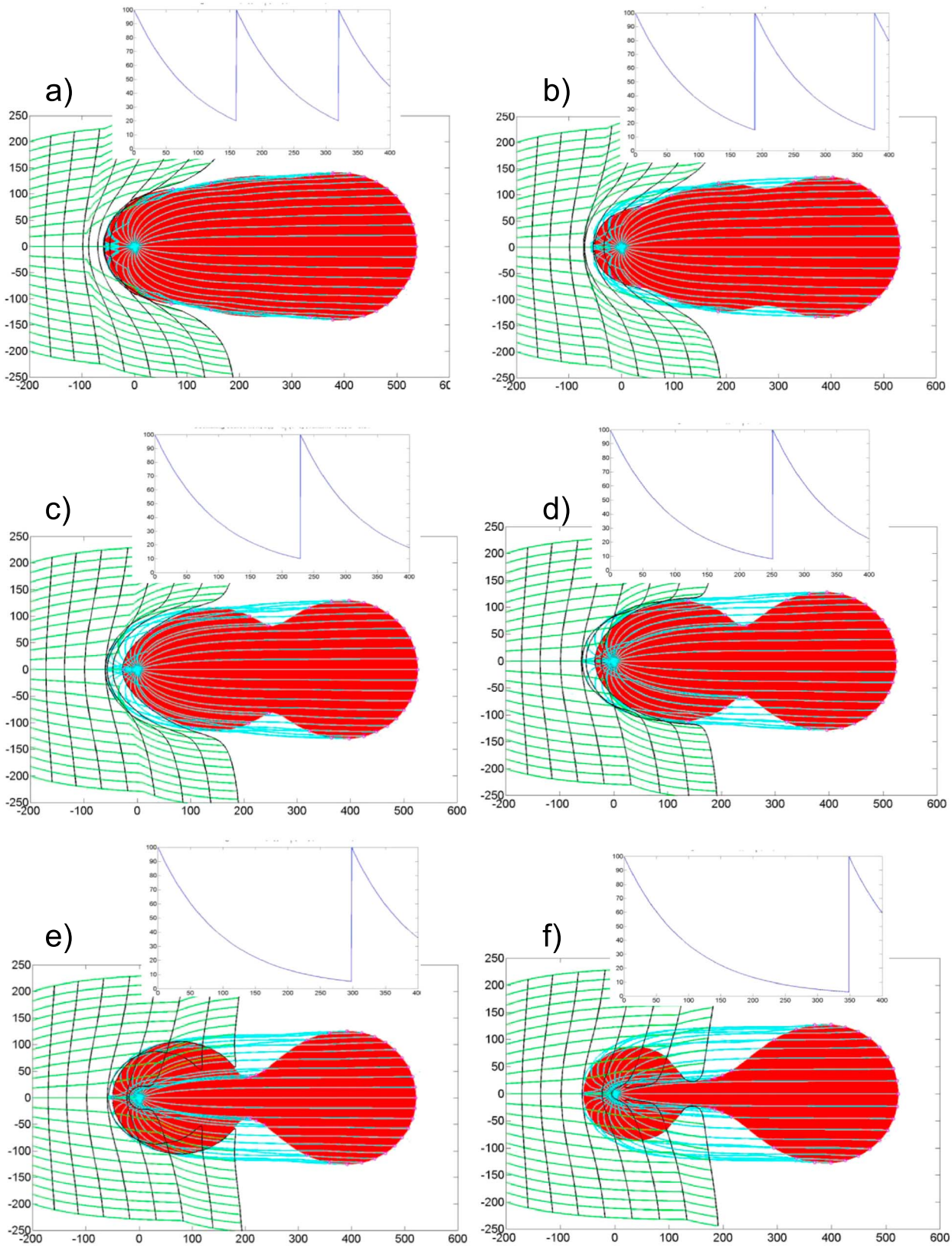

Figure 23. (a–f) Comprehensive overview of different final plume shapes resulting from oscillating source flow rates. Curves for oscillating *Rk* values shown above final shapes resulting after at total run time *t** of 600 nondimensional time. In all animations, time contours spaced for 50 nondimensional time-lapse intervals. Nondimensional field of view, scaled relative to unit length, is 1000 by 500. MATLAB models generated from our analytical flow equations.

©2014. American Geophysical Union. All Rights Reserved.

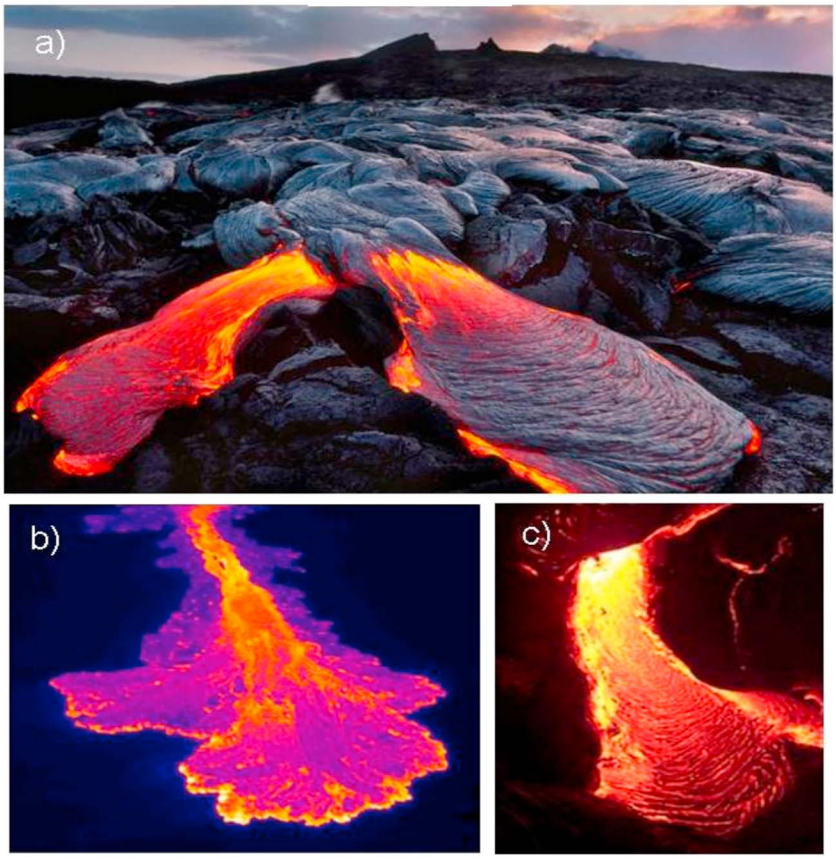

Figure 24. (a) Pillow lava plumes at Kilauea (courtesy Luci Yamamoto, Lonely Planet). (b) Thermal image of major Kilauea lava stream (courtesy USGS Hawaiian Volcano Observatory, March 2011). (c) Night image Kilauea lava (courtesy Bruce Applegate, April 2000).

numbers (due to high viscosity of ice) and only slowly declining source strength ($0 < \alpha < 1$), as summarized in our models of Figures 20a–20c (top row).

Other glaciers may have formed by a relatively steady supply of ice from their valley channels (i.e., $\alpha \rightarrow 1$). This conclusion is based on the appearance of Malaspina ice glacier in southeastern Alaska, a compound piedmont glacier fed by glaciers flowing from ice fields in the Saint Elias Mountains (Figure 25). The glacier

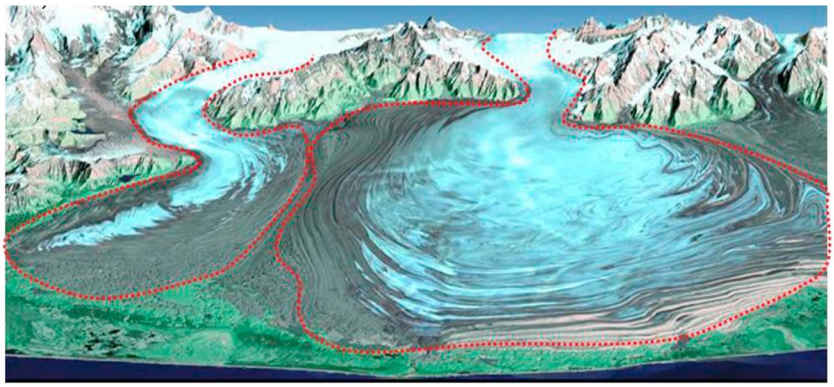

Figure 25. Perspective view of Malaspina Glacier (right, outlined by red dots) and adjacent Agassiz Glacier (left, red dots), created from Landsat satellite image and elevation model generated by Shuttle Radar Topography Mission. Vertical exaggeration = 2X; view due north. Data were taken on 11 February 2000. (Image URL: http://photojournal.jpl.nasa.gov/catalog/pia03386.)

©2014. American Geophysical Union. All Rights Reserved.

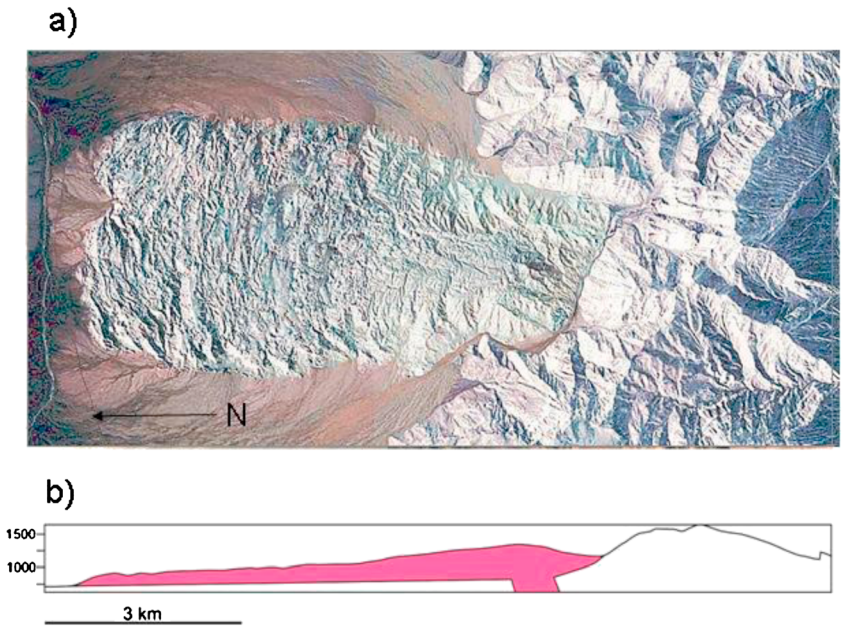

Figure 26. (a) False color satellite image of Siah Tagh salt glacier, Zagros Mountains, SW Iran (27.51°N, 54.57°E). This salt glacier is also visible in central part of Figure 1 (courtesy Google Earth). (b) Geological cross section of salt glacier in Figure 26a.

flows from its confining valleys onto a coastal plain and forms an eggplant shape (term defined in Figure 20), which is typical for high *Rk* number flows with little decline of source strength. The internal folds are clear evidence that plastic deformation is a strong component of glacial flow, and moraines line the margins of the glacier. The Malaspina Glacier extends up to 45 km (28 miles) from the mountain front nearly to the sea. Malaspina Glacier is flanked by the Agassiz Glacier (to its left, W side), from which it is separated by an interlobate ridge of moraine material. The Agassiz Glacier has a similar eggplant shape (Figure 25).

Our study was initially started to develop a simple geomechanical model that could explain the shape evolution of salt glaciers in Iran (Figure 1). A magnified image of the Siah Tagh salt sheet (Figure 26a) shows that the salt mass issued from the Siah Tagh feeder stock has become elongated, due to the superposed downslope flow, into a mature torpedo-shaped salt sheet (as in the model flow of Figure 20b, top). Our modeling insight can be used to confirm that natural salt sheets like Siah Tagh are emplaced with relatively modest (but steady) decline in source strength ($0 < \alpha < 1$).

As a general observation we conclude that ice glaciers (Figures 2 and 25) and salt glaciers (Figures 1 and 26) both exhibit gravity flows that develop into sheets with shapes confined to eggplant, pear, torpedo, club, and possibly cigar (terms and shapes in Figure 20). This is very unlike volcanic mud flows (Figures 18) and lava flows (Figure 24) which may develop plumes shaped like pendulum, teardrops, and tadpoles (Figure 20). The latter shapes are typical for gravity flows of relatively low viscosity materials erupting by one or several pluses, followed by a rapid decline in source strength. High-viscosity ice and salt glaciers generally emplace with higher Rankine numbers than volcanic mud and lava flows. The latter flows have relatively lower viscosities and therefore lower Rankine number flow shapes.

Some caution must be taken in inferring flow dynamics from a single shape observation in nature, as follows from an additional time series of our models for the development of eggplant- and pear-shaped plumes typical for ice and salt sheets (Figure 27). The two model flows of Figures 27a and 27b are in their early stages indistinguishable. The flow outlines of mature gravity flows will be diagnostic for its flux decline rate. Furthermore, some circular pancake-shaped salt glaciers in Iran, such as the Syahoo salt diapir (Figure 7b), indicate increasing source flux strengths ($\alpha > 1$). We have run an additional suite of models simulating plumes developing on slopes with an initially waxing source strength pattern (summarized in Appendices C and D), which develop typical plume shapes different from Figures 20a–20c. These complementary shapes are classified here as egg- and flying saucer-shaped plumes for easy reference to its diagnostic features. What is characteristic for such flows with initially increasing source flux strengths ($\alpha > 1$) is that their leading edges are

©2014. American Geophysical Union. All Rights Reserved.

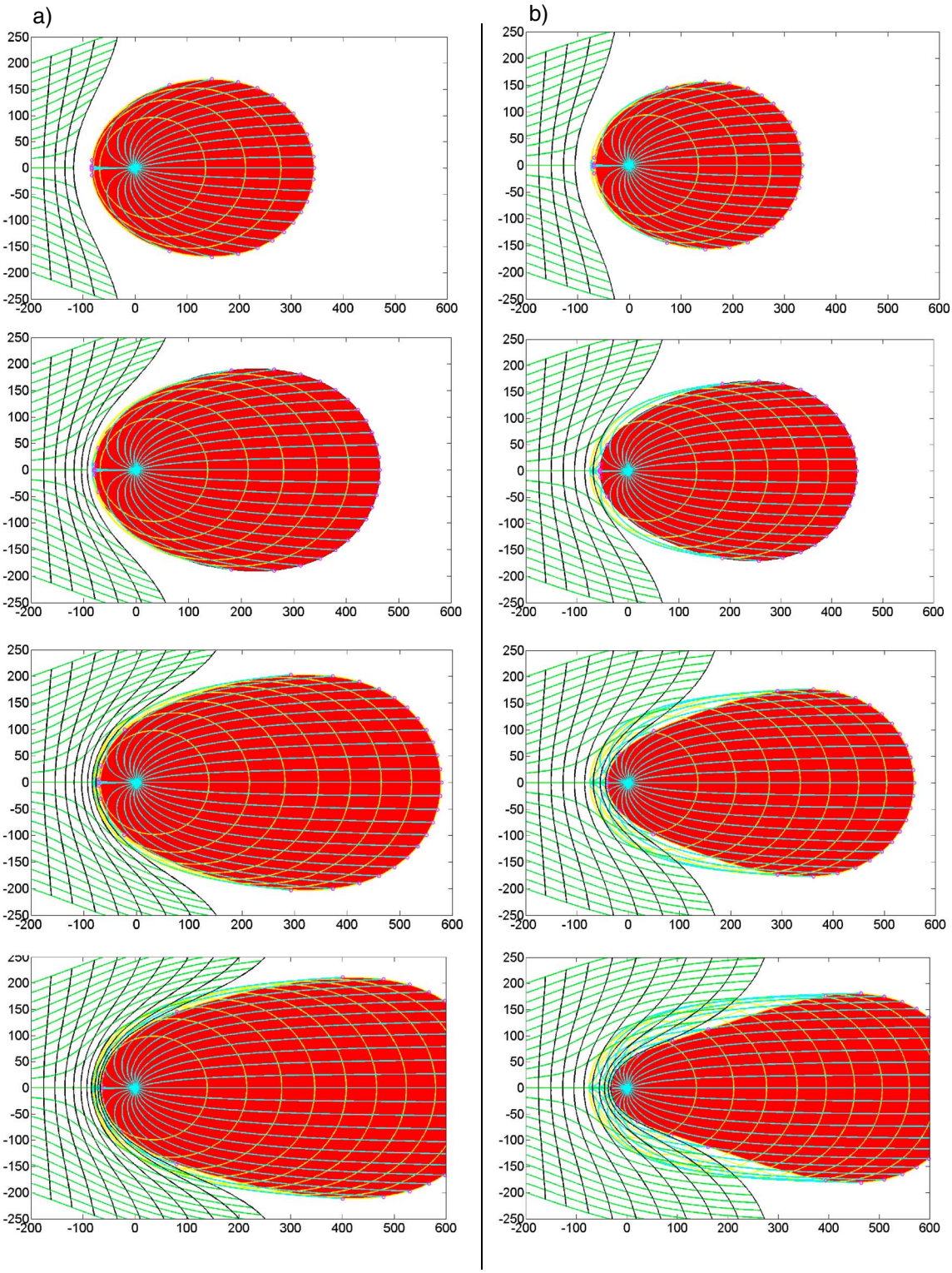

Figure 27. Time series for the evolution of source flow shapes for time-dependent decline of source flow rate (time-dependent *b* values). (a) Eggplant-shaped plume for initial *Rk* value of 100 and decline rate −0.001. (b) Pear-shaped plume for initial *Rk* value of 100 and faster decline rate: 0.0025. Run times from top to bottom rows: $t^* = 200$, 300, 400, and 500 nondimensional time units. Corresponding decline curves are included in Figure 20. Time contours spaced for 50 nondimensional time steps. Nondimensional field of view, scaled relative to unit length, is 500 by 800. Flow line spacing of source flows reduced for lower *b* numbers to avoid clustering of lines. MATLAB models generated from our analytical flow equations.

©2014. American Geophysical Union. All Rights Reserved.

narrower. This is unique for source fluxes $\alpha > 1$, which result in plume shapes narrowing in downslope direction (Figures C1, C2, and D2). In contrast, gravity flows developing from sources with declining flux strengths ($\alpha < 1$) evolve with plume shapes narrowing in upslope direction (Figures 20 and 27).

7. Conclusions

This study has simulated point-sourced gravity flows of Earth materials spreading over subplanar slopes using analytical flow descriptions based on Rankine flow equations. The approximation of the radial velocity profile by a 2-D axisymmetric Hele-Shaw source flow is a deliberate simplification to facilitate modeling, including time-dependent changes in source strength. The shape of the plumes around source flows on a slope is determined by the relative strength of the source flux and the downslope flow rate. The ratio of the two rates divided by a characteristic length scale is defined here as the Rankine number (*Rk*). This dimensionless number remains constant for sources having a steady source flux strength on a constant slope. The weaker the source flux strength, the narrower a plume will evolve. For $Rk = 1$, the plume becomes a narrow streak; for $Rk = 100$ (source flux strength 100 times that of the far-field flow rate) a broad, expanding plume evolves.

Natural gravity flows commonly have unsteady source fluxes; the volumetric flux strength is not constant over time ($\alpha \neq 1$). Our study included models for a range of declining flux strengths ($\alpha < 1$), which can generate a wide range of plume shapes, depending upon the starting *Rk* value and subsequent decline rate of the source flux. By systematically varying the initial *Rk* and decline rates, a range of possible plume shapes has been simulated. For ease of use in applications to natural flows, simple geometrical terms have been proposed to describe the range of plumes seen in our models: eggplant, pear, racket, torpedo, club, cigar, carrot, tadpole, teardrop, and pendulum shapes (see Figure 20 for summary).

Volcanic mud flows generally have shapes characteristic of gravity flows having lower effective viscosities (tadpole- and racket-shaped plumes), whereas lava flows exhibit racket-, club-, and carrot-shaped plumes. The lower Rankine number shapes occur for lower viscosity material. The effect of magmatic pulses on a lava field has been modeled to explain the undulating width of La Poruña lava field in the Chilean Andes.

Crystalline creep of ice glaciers onto piedmonts typically develops into immature or mature eggplant, club, and torpedo shapes. Mature eggplant plume shapes apply to the Malaspina and Agassiz ice glaciers (SE Alaska; Figure 25), Elephant Foot Glacier (Greenland; Figure 2a), and unconstrained terminal tongues of ice glaciers on Axel Heiberg Island (Canada; Figure 2b).

Subaerial salt glaciers typically develop torpedo shapes when on a slope (Siah Tagh salt sheet, Iran; Figure 26) and pancakes when a regional slope is negligible (Syahoo salt diapir, Iran; Figure 7c). Future work applies our model to explain the formation of subaqueous salt sheets near the Mississippi Delta (e.g., Mitchell, Farnella, Gloria, and Whiting domes) and analyzes how these spread under gravity down the continental slope of the Gulf of Mexico. The model has also been successfully applied to reconstruct the emplacement of Chao dacite complex from three source vents along a fracture that started to emit magma as the fracture propagated [*Weijermars*, 2014]. The examples given in our present and related studies provide evidence that Rankine flow models can be successfully applied to model the overall planform evolution of gravity flows on a slope.

Appendix A: Viscous Applications of Stream Function Solutions

The Navier-Stokes equation for an incompressible fluid (constant density ρ) and Newtonian dynamic viscosity μ can be expressed in terms of the Jacobian determinant using a stream function ψ:

$$\frac{\partial}{\partial t}\nabla^2\psi + \frac{\partial(\psi, \nabla^2\psi)}{\partial(x, y)} - \nu\nabla^4\psi = 0 \tag{A1}$$

This assumes that there are no other body forces other than those due to a pressure gradient. The kinematic viscosity ν (=μ/ρ, with density ρ) accounts for constant material properties of the fluid continuum. The first two terms in equation (A1) are inertia terms, which vanish in creeping flow so that the Jacobian flow descriptor becomes

$$\nu\nabla^4\psi = 0 \tag{A2}$$

©2014. American Geophysical Union. All Rights Reserved.

When fluid viscosity is scaled out, equation (A2) can be further simplified to

$$\nabla^4 \psi = 0 \tag{A3}$$

The description may still apply to viscous flow, and the viscosity may have any possible value, but remains constant throughout a given flow space. Scaling the viscosity out at this stage provides a concise flow description.

The stream function description of fluid flow was normalized by the viscosity (see equations (A2) and (A3)), which often is represented as a description of nonviscous flow. This section shows how the so-called "inviscous description" still contains the strain rate and can be redimensionalized to provide a constitutive relationship between stress and strain rate. The velocity gradient tensor can be expressed in terms of the stream function:

$$\nabla V = \begin{bmatrix} \dfrac{\partial^2 \psi}{\partial x \partial y} & \dfrac{\partial^2 \psi}{\partial y^2} \\ -\dfrac{\partial^2 \psi}{\partial x^2} & -\dfrac{\partial^2 \psi}{\partial y \partial x} \end{bmatrix} \tag{A4}$$

The decomposition in the symmetric and the antisymmetric part gives

$$\nabla V = \begin{bmatrix} \dfrac{\partial^2 \psi}{\partial x \partial y} & \dfrac{1}{2}\left(\dfrac{\partial^2 \psi}{\partial y^2} - \dfrac{\partial^2 \psi}{\partial x^2}\right) \\ \dfrac{1}{2}\left(\dfrac{\partial^2 \psi}{\partial y^2} - \dfrac{\partial^2 \psi}{\partial x^2}\right) & -\dfrac{\partial^2 \psi}{\partial y \partial x} \end{bmatrix} + \begin{bmatrix} 0 & \dfrac{1}{2}\left(\dfrac{\partial^2 \psi}{\partial y^2} + \dfrac{\partial^2 \psi}{\partial x^2}\right) \\ -\dfrac{1}{2}\left(\dfrac{\partial^2 \psi}{\partial y^2} + \dfrac{\partial^2 \psi}{\partial x^2}\right) & 0 \end{bmatrix} \tag{A5}$$

The first matrix is the strain rate tensor E, and the second matrix is the rigid rotation rate tensor W.

The principal strain rates in terms of the stream function are

$$e_1, e_2 = \pm \frac{1}{2} \sqrt{\left(\frac{\partial^2 \psi}{\partial x \partial y} + \frac{\partial^2 \psi}{\partial x \partial y}\right)^2 + \left(\frac{\partial^2 \psi}{\partial y^2} - \frac{\partial^2 \psi}{\partial x^2}\right)^2} \tag{A6}$$

The maximum shear strain rate is

$$e_{xy,\max} = \frac{1}{2} \sqrt{\left(\frac{\partial^2 \psi}{\partial x \partial y} + \frac{\partial^2 \psi}{\partial x \partial y}\right)^2 + \left(\frac{\partial^2 \psi}{\partial y^2} - \frac{\partial^2 \psi}{\partial x^2}\right)^2} \tag{A7}$$

The total stress tensor for incompressible viscous flow is

$$\sigma_{ij} = -p\delta_{ij} + \tau_{ij} \tag{A8}$$

The static pressure p is due to uniform compression, and the deviatoric or viscous stress tensor τ_{ij} account for the viscous flow resistance of the fluid continuum. The viscous stress τ_{ij} depends on gradients of velocity and vanishes if there is no velocity gradient (uniform flow). The original flow description can now be dimensionalized by adopting equation (A2), valid for a fluid continuum with a specific viscosity. The preferred viscosity measure to express shear resistance is the dynamic viscosity μ:

$$\tau_{ij} = 2\mu \begin{bmatrix} \dfrac{\partial^2 \psi}{\partial x \partial y} & \dfrac{1}{2}\left(\dfrac{\partial^2 \psi}{\partial y^2} - \dfrac{\partial^2 \psi}{\partial x^2}\right) \\ \dfrac{1}{2}\left(\dfrac{\partial^2 \psi}{\partial y^2} - \dfrac{\partial^2 \psi}{\partial x^2}\right) & -\dfrac{\partial^2 \psi}{\partial y \partial x} \end{bmatrix} \tag{A9}$$

©2014. American Geophysical Union. All Rights Reserved.

The deviatoric stresses τ_{xx} for any point in the flow follows from the principal strain rate in a constitutive relationship:

$$\tau_{ij} = 2\mu e_{ij} \tag{A10}$$

The dynamic viscosity μ accounts for viscous resistance of the fluid continuum.

Appendix B: Equations

Source flows enjoy the attention of applied mathematicians because such flows can be described by concise functions with analytical solutions. Streamlines may be visualized by mapping complex contour integrals using the vector field representation with conformal mapping of complex variables, as formalized by Pólya [*Pólya and Latta*, 1974]. A similar method has been used in fluid mechanics, using complex functions for concise mathematical representation of the potential function and the stream function [*Batchelor*, 1967; *Weijermars and Poliakov*, 1993; *Kundu and Cohen*, 2002]. These functions can describe the physical transport of particles in basic flow fields (vortices, sources, sinks, doublets, and uniform flows).

Assuming a stream function ψ that provides a valid solution of the Navier-Stokes equation for a particular flow (Appendix A, equation (A1)), a valid potential function, ϕ, follows from ψ:

$$\frac{\partial \psi}{\partial y} = \frac{\partial \phi}{\partial x} \tag{B1a}$$

$$\frac{\partial \psi}{\partial x} = -\frac{\partial \phi}{\partial y} \tag{B1b}$$

A good number of flow patterns can be described by an appropriate pair of potential functions and stream functions that satisfy the Cauchy-Riemann equations. When satisfied, these equations imply that divergence and curl are negligibly small. The key property of analytical functions of complex line integrals is that the complex variables map the spatial position of the complex function; the variables also describe valid solutions for the fluid flow in each position. For detailed definitions of the analytical functions and line integrals, see *Needham* [1967, pp. 197 and 383, respectively]. To be valid, the analytical description requires (1) conservation of mass, which requires divergence to be zero and assumes incompressibility and (2) irrotational flow so that vorticity (also termed curl or circulation) is zero. Advanced numerical analyses of nonlinear flow solutions can solve the differential equations by approximate solutions [*Anderson*, 1995]. As a result, fluid mechanics has shifted from analytical solutions for linear flow (exact solutions of approximate flow descriptions) to numerical methods for solving nonlinear differential equations (approximate solutions of exact problems [*Drazin and Riley* 2006]). Nonetheless, describing fluid flow by exact solutions of the Navier-Stokes equation elucidates the fundamentals of fluid flow [*Barenblatt*, 1996]. Analytical equations therefore remain useful for description of laminar flow in geologic systems that lack inertia effects [*Weijermars and Schmeling*, 1986].

B1. Complex Potential

The description of source flows in terms of complex functions enjoys a revived interest in applied mathematics [*Churchill and Brown*, 1984; *Potter*, 2008; *Zill and Shanahan*, 2009; *Brilleslyper et al.*, 2012]. We adopt the complex function $F(z)$ with independent variable $z = x + iy$, where $i = \sqrt{-1}$:

$$F(z) = \varphi(x, y) + i\psi(x, y) \tag{B2}$$

with potential function $\varphi(x, y)$ and stream function $\psi(x, y)$ as the real part $\Re(z)$ of z and the imaginary part $\Im(z)$ of z (which can be obtained by multiplying the real number with i).

The conditions of incompressible and irrotational flow are fulfilled when $\nabla^2\varphi = 0$ and $\nabla^2\psi = 0$, meaning that both φ and ψ are harmonic functions. The derivative of $F(z)$ with respect to z gives the vector field, which in Cartesian coordinates is given by

$$V(z) = \mathrm{d}F/\mathrm{d}z = \frac{\partial \phi}{\partial x} + i\frac{\partial \psi}{\partial x} = u_x - iu_y \tag{B3a}$$

©2014. American Geophysical Union. All Rights Reserved.

And in plane-polar coordinates

$$V(z) = (u_r - iu_\theta)\exp(-i\theta) \tag{B3b}$$

The spatial velocity vectors are respectively given by (u_x,u_y) and (u_r, u_θ).

B2. Application to Source Flow

A single-source flow located at $z = 0$ (the origin) is given by the complex potential (using $z = |z|e^{i\theta}$ with modulus $|z| = r$)

$$W(z) = m\ \log(z) = \ m\ \ln(z)\ = m\ \ln\left(re^{i\theta}\right) \tag{B4}$$

$$V(z)\ =\ m/z\ = m/\left(re^{i\theta}\right) \tag{B5}$$

with strength $m = Q/2\pi r$ (for $r \sim 1$) with total fluid volume Q_{tot} generated at any radius equal to $Q_{tot} = m2\pi\ r$ (and with dimension [$m^2\ s^{-1}$], due to unit length in the third dimension; fluid emerging from a diapiric stock of horizontal cross-sectional area πr^2 flows at a rate $Q = U_{mean}\ \pi r^2$ [$m^3\ s^{-1}$]).

Comparing equations (B3b) and (B5) reveals that the components of the velocity field are

$$u_r = \ m/r \tag{B6a}$$

$$u_\theta = \ 0 \tag{B6b}$$

The corresponding stream functions and potential functions in Cartesian coordinate are

$$\varphi(x,\ y)\ = (1/2)\ m\ \ln\left(x^2 + y^2\right) \tag{B7a}$$

$$\psi(x,\ y) = \ m\ \tan^{-1}\qquad (y/x) \tag{B7b}$$

and in polar coordinates (using $r^2 = x^2 + y^2$ and $\theta = \tan^{-1}(y/x)$):

$$\varphi(r,\theta) = \ m\ \ln r \tag{B8a}$$

$$\psi(r,\theta) = \ m\theta \tag{B8b}$$

Equations (B7a), (B7b), (B8a), and (B8b) fulfill the conditions $\nabla^2\varphi = 0$ and $\nabla^2\psi = 0$.

B3. Application to Far-Field Flow

For a uniform flow with velocity components (u_x,u_y) the corresponding stream functions and potential functions in Cartesian coordinates are

$$\varphi(x,y) = u_x x + u_y y \tag{B9a}$$

$$\psi(x,y) = u_x y - u_y x \tag{B9b}$$

The superposed uniform flow and the source flow are given by adding the potential and stream function descriptions flow field given in equations B8a, B8b, B9a, B9b. The result is given below, with hybrid notation in polar and Cartesian coordinates for practical convenience:

$$\varphi = u_x x + u_y y + m\ln r \tag{B10a}$$

$$\psi = u_x y - u_y x + m\theta \tag{B10b}$$

We can take x and y derivatives of this flow field to compute the velocity field. The distance, d, between the point source (x_s,y_s) and a general point (x,y) is

$$d = \sqrt{(x - x_s)^2 + (y - y_s)^2} \tag{B11}$$

©2014. American Geophysical Union. All Rights Reserved.

Thus, taking into account where the source has been placed, the velocity potential, in Cartesian form, is

$$\varphi(x,y) = (m/2)\ln\left[(x-x_s)^2 + (y-y_s)^2\right] + u_x x + u_y y \tag{B12}$$

and the velocities are

$$u_x = \frac{\partial\varphi}{\partial x} = \frac{m}{4}\frac{(x-x_s)}{(x-x_s)^2 + (y-y_s)^2} + u_x \tag{B13a}$$

$$u_y = \frac{\partial\varphi}{\partial y} = \frac{m}{4}\frac{(y-y_s)}{(x-x_s)^2 + (y-y_s)^2} + u_y \tag{B13b}$$

The dimensional description of the uniform far-field flow is given by U_∞ in polar coordinates (r, θ) and is given by

$$\psi(r,\theta) = U_\infty r \sin\theta \tag{B14}$$

B4. Superposition of Far-Field Flow and Source Flow

Superposition of the stream function for a far-field flow (equation (B14)) with the stream function of the source flow (equation (B8b)) gives the expression for Rankine flow around a half body:

$$\psi(r,\theta) = U_\infty r \sin\theta + m\theta \tag{B15}$$

The dimensional velocity field is given by

$$u_x = \frac{\partial\psi}{\partial y} = U_\infty + (m/r)\cos\theta \tag{B16a}$$

$$u_y = -\frac{\partial\psi}{\partial x} = (m/r)\sin\theta \tag{B16b}$$

These functions are used as the basis for a particle path tracing that lead to the results in the main text.

Appendix C: Egg Shapes for Increasing Source Rates ($\alpha > 1$; Logarithmic and Exponential *Rk*)

The upstream pointed plume shapes form when sources extruding fluid at constant or declining flux strengths (Figure 20). If the source flux progressively decelerates, egg-shaped plumes form with their narrower ends directed downstream; all forms shown are for runtime 600 but the differences in specific shape result from the specific inflation-rate profile of the flux strength (see graphs in second row from the bottom, Figure C1a). Similar egg-shaped plumes, but pointing downslope, evolve for progressively accelerating flux strengths (Figure C1b). This geometry provides a criterion to interpret from a plume shape of a natural mass flow whether the source extruded at increasing or decreasing rates. Figures C2a and C2b show time series for the most striking examples of egg-shaped salt sheets extruding at accelerating flow rates.

Appendix D: Flying Saucer Shapes for Bell Curve Source Rates (First $\alpha > 1$ Then $\alpha < 1$)

Natural source flows cannot accelerate exponentially indefinitely. For example, pipe flow physics and the finite volume of the source layer of mud and lava flows suggest that extrusion rates could rise slowly before declining. This kind of bell-shaped change in flux strengths could result in plumes having a flying saucer-shape (Figure D1). Figures D2a and D2b show time series for the most striking examples of flying saucer-shaped plumes.

©2014. American Geophysical Union. All Rights Reserved.

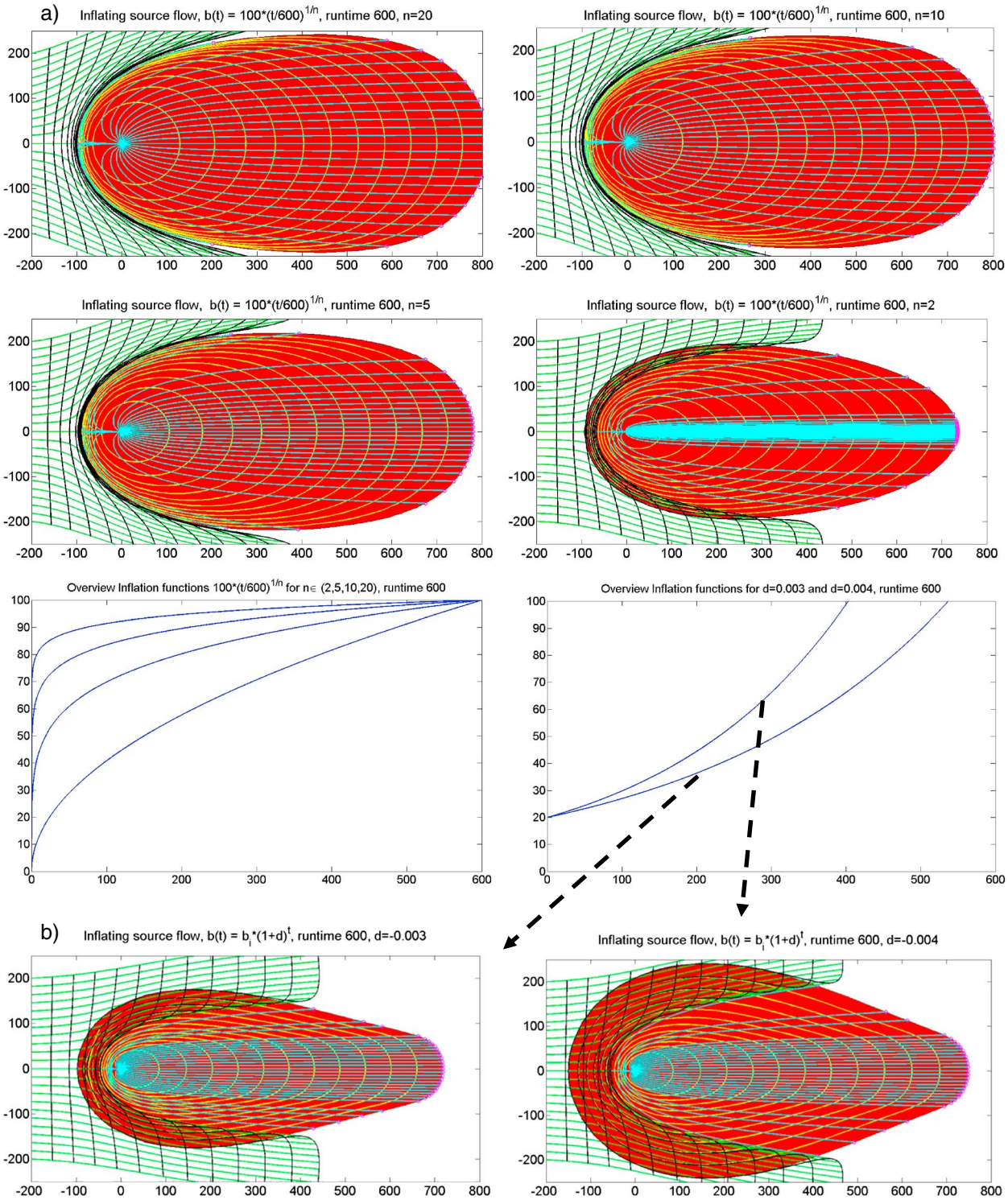

Figure C1. Final plume shapes for time-dependent growth of source flow rate (time-dependent *Rk* values). (a) Top four animations are final shapes for logarithmic growth of source rate. (b) Bottom two animations are final shapes for exponential growth of source rate. Corresponding *Rk* value curves are graphed in the bottom row of Figure C1a (left, logarithmic growth in source strength; right, exponential growth of source strength). In all graphs, time contours spaced for 50 nondimensional time steps. Total run time = 600 nondimensional time steps. Nondimensional field of view, scaled relative to unit length, is 1000 by 450. MATLAB models generated from our analytical flow equations.

©2014. American Geophysical Union. All Rights Reserved.

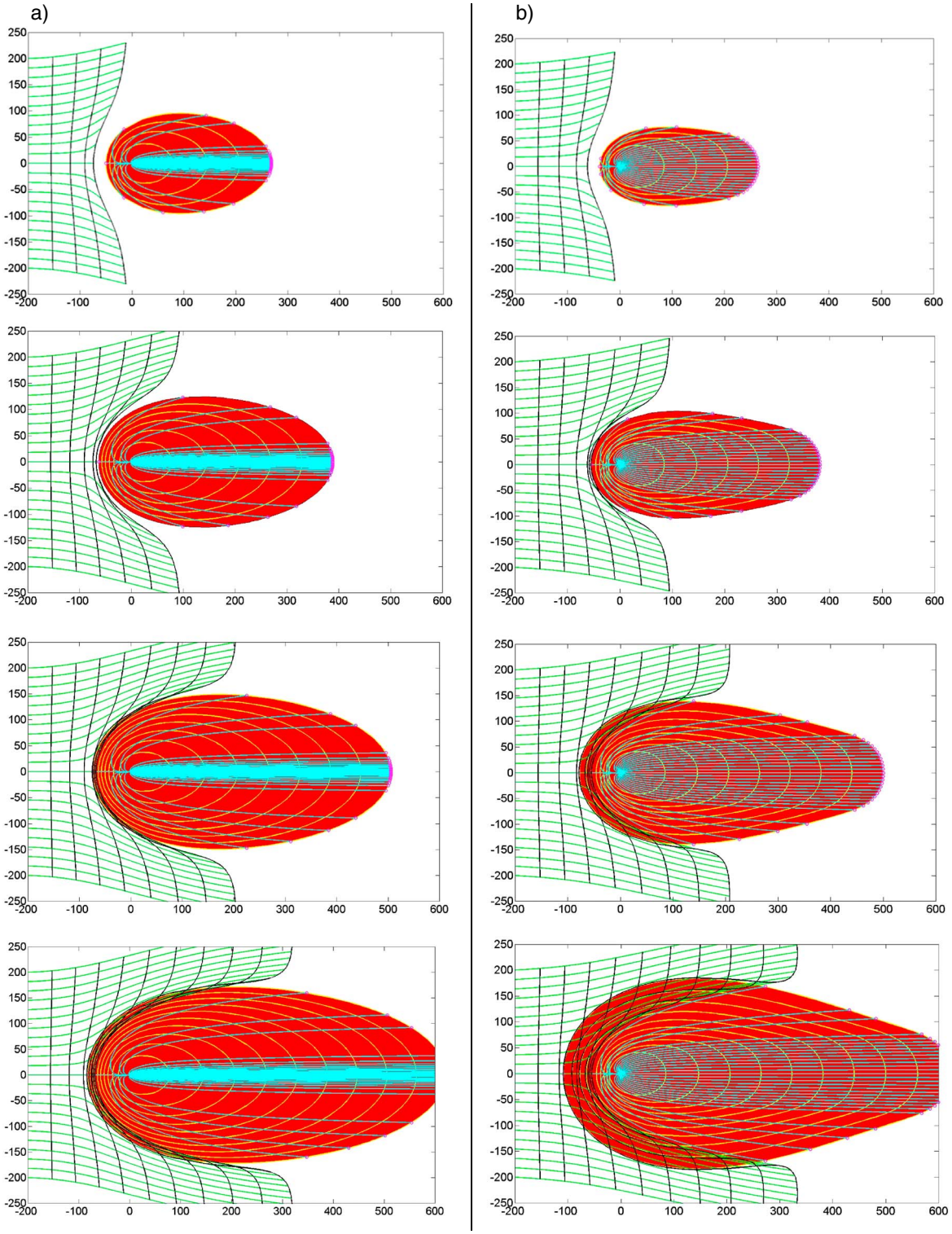

Figure C2. Time series for the evolution of plume shapes for time-dependent increase of source flow rate (time-dependent *b* values). (a) Left-hand column for growth with logarithmic deceleration of flux strength toward maximum rate. (b) Right-hand column for source flux growth with exponential increase. Run times from top to bottom rows: $t^* = 200$, 300, 400, and 500 nondimensional time units. Corresponding decline curves are given in the third row of Figure C1. Time contours spaced for 50 nondimensional time steps. Nondimensional field of view, scaled relative to unit length, is 800 by 500. MATLAB models generated from our analytical flow equations.

©2014. American Geophysical Union. All Rights Reserved.

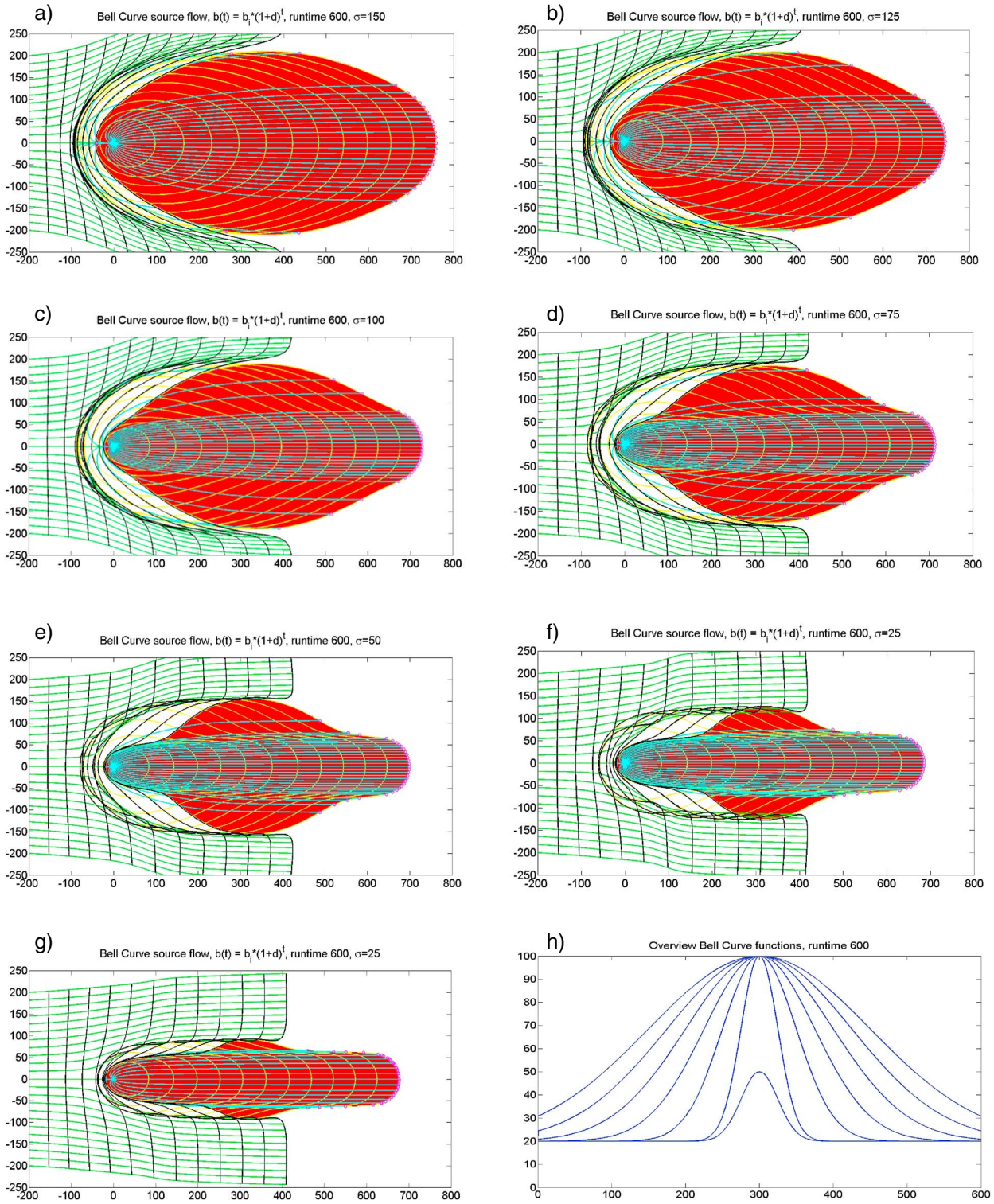

Figure D1. (a–h) Different final plume shapes resulting from time-dependent growth and decline of source flow rate (time-dependent *b* values). Corresponding bell curves for *Rk* values shown in right-hand graph at bottom row for sigma values of 150, 125, 100, 75, 50, 25 (for $Rk_{max} = 100$) and one run for $Rk_{max} = 50$ with sigma = 25. Total run time: $t^* = 600$ nondimensional time and time contours in all animations spaced for 50 nondimensional time-lapse intervals. Nondimensional field of view, scaled relative to unit length, is 1000 by 500. MATLAB models generated from our analytical flow equations.

©2014. American Geophysical Union. All Rights Reserved.

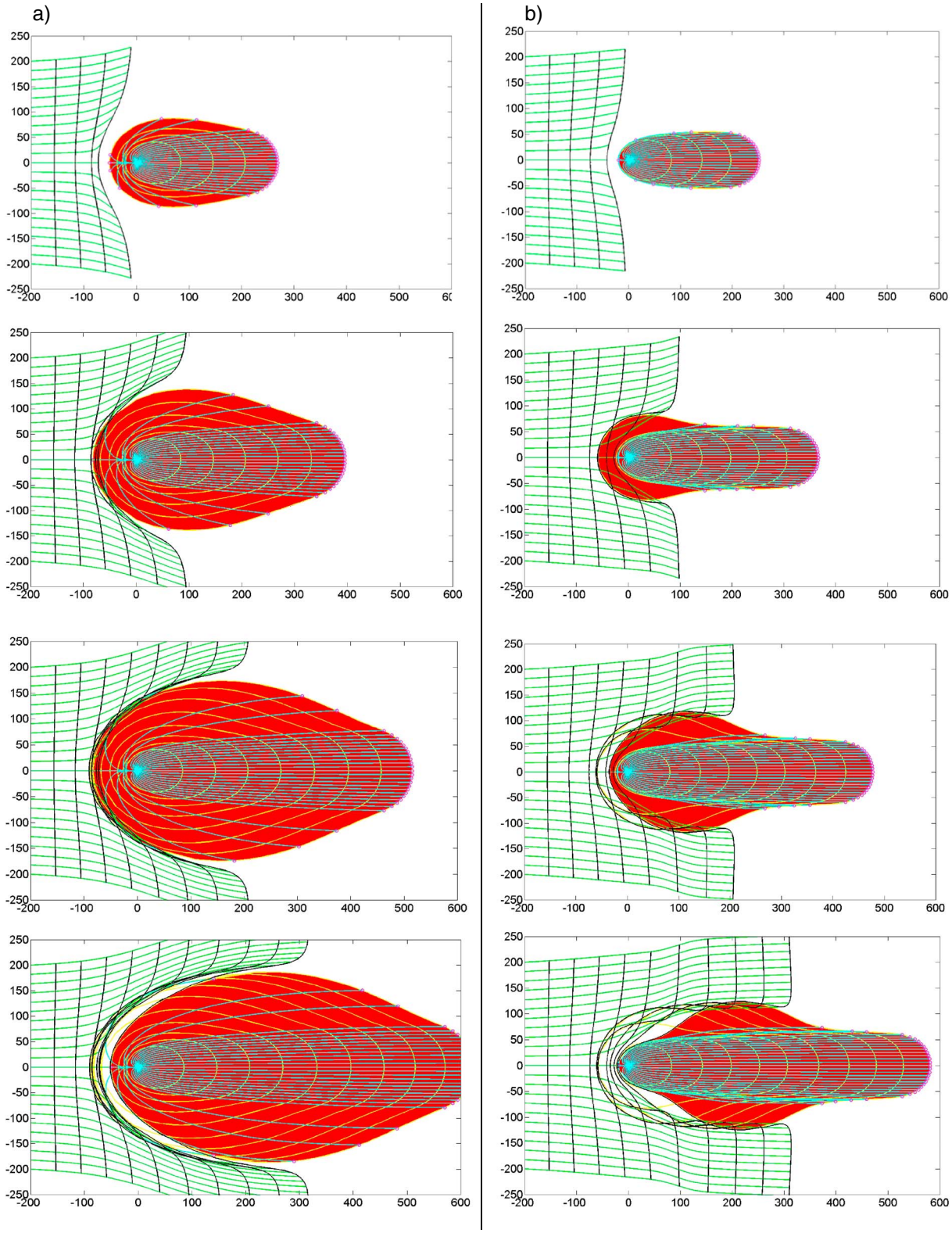

Figure D2. Time series for the development of plume shapes for bell curve evolution of source flow rate (time-dependent *Rk* values). (a) Left-hand column is for rise and fall of source flow rate following bell curve with spread sigma of 100 and maximum *Rk* value of 100. (b) Right-hand column is for rise and fall of source flow rate following bell curve with spread sigma of 25 and maximum *Rk* value of 100. Corresponding bell curves included in lower right-hand graph of Figure D1. Run times from top to bottom rows: $t^* = 200$, 300, 400, and 500 nondimensional time units. Time contours spaced for 50 nondimensional time-lapse intervals. Nondimensional field of view, scaled relative to unit length, is 800 by 500. MATLAB models generated from our analytical flow equations.

©2014. American Geophysical Union. All Rights Reserved.

Acknowledgments
This research was funded by the Applied Geodynamics Laboratory consortium and by the Jackson School of Geosciences. Dave Waltham and several anonymous reviewers provided insightful reviews and suggestions for improvement. Arnaud van Harmelen is gratefully acknowledged for his support with MATLAB coding. Chris Parker edited the paper. The Director, Bureau of Economic Geology, authorized the publication. The data to support this article are from the AGL research consortium. Because of proprietary reasons, the data cannot be released.

References

Aloisi, G., C. Pierre, J.-M. Rouchy, J.-P. Foucher, J. Woodside, and M. S. Party (2000a), Methane-related authigenic carbonates of eastern Mediterranean Sea mud volcanoes and their possible relation to gas hydrate destabilisation, *Earth Planet. Sci. Lett.*, *184*, 321–338.

Aloisi, G., C. Pierre, J.-M. Rouchy, J.-P. Foucher, J. Woodside, and M. S. Party (2000b), Linking Mediterranean brine pools and mud volcanism, *Eos Trans. AGU*, *81*(5), 625–632.

Anderson, J. D. (1995), *Computational Fluid Dynamics: The Basics With Applications*, McGraw-Hill, New York.

Barenblatt, G. I. (1996), *Scaling, Self-Similarity and Intermediate Asymptotics*, Cambridge Univ. Press, Cambridge, U. K.

Batchelor, G. K. (1967), *An Introduction to Fluid Mechanics*, Cambridge Univ. Press, Cambridge, U. K.

Betelu, S., J. Diez, L. Thomas, R. Gratton, and B. Marino (1997), A boundary element method for viscous gravity currents, *Int. J. Numer. Methods Fluids*, *25*, 1–19.

Birman, V. K., and E. Meiburg (2006), High-resolution simulation of gravity currents, *J. Braz. Soc. Mech. Sci. Eng.*, *28*(2), 169–173.

Brilleslyper, M. A., M. A. Dorff, J. M. McDougall, J. Rolf, L. E. Schaubroeck, R. L. Stankewitz, and K. Stephenson (2012), *Explorations in Complex Analysis*, Mathematical Association of America Inc., MAA Service Center, Washington, D. C.

Brun, J. P., and O. Merle (1985), Strain patterns in models of spreading-gliding nappes, *Tectonics*, *4*(7), 705–719, doi:10.1029/TC004i007p00705.

Bush, J. W. M., J. M. Aristoff, and A. E. Hosoi (2006), An experimental investigation of the stability of the circular hydraulic jump, *J. Fluid Mech.*, *558*, 33–52.

Churchill, R. V., and J. W. Brown (1984), *Complex Variables and Applications*, 4th ed., McGraw-Hill Book Company, New York.

De Lange, G. J., and H.-J. Brumsack (1998), Pore water indications for the occurrence of gas hydrates in eastern Mediterranean mud dome structures, in *Proceedings of the ODP, Scientific Results*, vol. 160, pp. 569–574, Ocean Drilling Program, College Station, Tex.

Didden, N., and T. Maxworthy (1982), The viscous spreading of plane and axisymmetric gravity currents, *J. Fluid Mech.*, *121*, 27–42.

Dimitrov, L. I. (2002), Mud volcanoes—The most important pathway for degassing deeply buried sediments, *Earth Sci. Rev.*, *59*, 49–76.

Drazin, P. G., and N. Riley (2006), *The Navier-Stokes Equations: A Classification of Flows and Exact Solutions*, Cambridge Univ. Press, Cambridge, U. K.

Fletcher, R. C., M. R. Hudec, and I. A. Watson (1995), Salt glacier and composite sediment-salt glacier models for the emplacement and early burial of allochthonous salt sheets, in *Salt Tectonics: A Global Perspective*, edited by M. P. A. Jackson, D. G. Roberts, and S. Snelson, pp. 77–108, AAPG Memoir 65.

Guliyev, I. S., and A. A. Feizullayev (1997), *All About Mud Volcanoes*, Nafta Press, Baku, Azerbaijan.

Hacker, J., P. F. Linden, and S. B. Dalziel (1996), Mixing in lock-release gravity currents, *Dyn. Atmos. Oceans*, *24*, 183–195.

Hovland, M., A. Hill, and D. Stokes (1997), The structure and geomorphology of the Dashgil mud volcano, Azerbaijan, *Geomorphology*, *21*, 1–15.

Huppert, H. E. (1982a), The propagation of two-dimensional and axisymmetric viscous gravity currents over a rigid horizontal surface, *J. Fluid Mech.*, *121*, 43–58.

Huppert, H. E. (1982b), Flow and instability of a viscous current down a slope, *Nature*, *300*, 427–429.

Huppert, H. E. (2006), Gravity currents: A personal perspective, *J. Fluid Mech.*, *554*, 299–322.

Huppert, H. E., and J. E. Simpson (1980), The slumping of gravity currents, *J. Fluid Mech.*, *99*, 785–799.

Joseph, D. D. (2003), Viscous potential flow, *J. Fluid Mech.*, *479*, 191–197.

Joseph, D. D. (2006), Potential low of viscous fluids: Historical notes, *Int. J. Multiphase Flow*, *32*, 285–310.

Joseph, D. D., and T. Y. Liao (1994), Potential flows of viscous and viscoelastic fluids, *J. Fluid Mech.*, *256*, 1–23.

Joseph, D. D., T. Funada, and J. Wang (2007), *Potential Flows of Viscous and Viscoelastic Liquids*, Cambridge Univ. Press, Cambridge, U. K.

Kadirov, F. A., and A. S. Mukhtarov (2004), Geophysical fields, deep structure, and dynamics of the Lokbatan mud volcano, *Izvestya Phys. Solid Earth*, *40*, 327–333.

Kopf, A. J. (2002), Significance of mud volcanism, *Rev. Geophys.*, *40*(2), 1005, doi:10.1029/2000RG000093.

Kundu, P. K., and I. M. Cohen (2002), *Fluid Mechanics*, 2nd ed., Academic Press, San Diego, Calif.

Lerche, I., and E. Bagirov (1998), Guide to gas hydrate stability in various geological settings, *Mar. Pet. Geol.*, *15*, 427–437.

Lister, J. R. (1992), Viscous flows down an inclined plane from point ad line sources, *J. Fluid Mech.*, *242*, 631–653.

Marshall, S. J. (2005), Recent advances in understanding ice sheet dynamics, *Earth Planet. Sci. Lett.*, *240*, 191–204.

Milkov, A. V. (2000), Worldwide distribution of submarine mud volcanoes and associated gas hydrates, *Mar. Geol.*, *167*, 29–42.

Needham, T. (1997), *Visual Complex Analysis*, Oxford Univ. Press, Oxford, U. K.

O'Callaghan, L. J., and P. W. Francis (1986), Volcanological and petrological evolution of San Pedro volcano, Provincia El Loa, North Chile, *J. Geol. Soc. Lond.*, *143*, 275–286.

Pólya, G., and G. Latta (1974), *Complex Variables*, Wiley, New York.

Potter, H. D. P. (2008), On conformal mappings and vector fields, Senior thesis, Marietta College, Marietta, Ohio.

Ramberg, H. (1981), *Gravity, Deformation and the Earth's Crust*, 2nd ed., Academic Press, London, U. K.

Scholte, K. H. (2005), Hyperspectral remote sensing and mud volcanism in Azerbaijan, PhD thesis, Delft Univ. of Technol., Netherlands.

Slim, A. C., and H. E. Huppert (2011), Axisymmetric, constantly supplied gravity currents at high Reynolds number, *J. Fluid Mech.*, *675*, 540–551.

Spera, F. J. (2000), Physical properties of magma, in *Encyclopedia of Volcanoes*, edited by H. Sigurdsson, pp. 171–189, Academic Press, San Diego, Calif.

Spurk, J. H., and N. Aksel (2008), *Fluid Mechanics*, 2nd ed., Springer, New York.

Svensen, H., D. A. Karlsen, A. Sturz, K. Backer-Owe, D. A. Banks, and S. Planke (2007), Processes controlling water and hydrocarbon composition in seeps from the Salton Sea Geothermal System, California, USA, *Geology*, *35*, 85–88.

Svensen, H., Ø. Hammer, A. Mazzini, N. Onderdonk, S. Polteau, S. Planke, and Y. Y. Podladchikov (2009), Dynamics of hydrothermal seeps from the Salton Sea geothermal system (California, USA) constrained by temperature monitoring and time series analysis, *J. Geophys. Res.*, *114*, B09201, doi:10.1029/2008JB006247.

Talbot, C. J. (1998), Extrusions of Hormuz salt in Iran, in *Lyell: The Past is the Key to the Present*, edited by D. J. Blundell and A. C. Scott, *Geol. Soc. London Spec. Publ.*, *143*, 315–334.

van Keken, P. E., C. J. Spiers, A. P. van Den Berg, and E. J. Muyzert (1993), The effective viscosity of rocksalt: Implementation of steady state creep laws in numerical models of salt diapirism, *Tectonophysics*, *225*, 457–475.

Wagner, B. H., III, and M. P. A. Jackson (2011), Viscous flow during salt welding, *Tectonophysics*, *510*, pp. 309–326, doi:10.1016/j.tecto.2011.07.012.

Weijermars, R. (1986), Polydimethylsiloxane flow defined for experiments in fluid dynamics, *Appl. Phys. Lett.*, *48*, 109–111.

Weijermars, R. (1988), Progressive fluid deformation in low Reynolds number flow past a falling cylinder, *Am. J. Phys.*, *56*, 534–540.

©2014. American Geophysical Union. All Rights Reserved.

Weijermars, R. (2014), Visualization of space competition and plume formation with complex potentials for multiple source flows: Some examples and novel application to Chao lava flow (Chile), *J. Geophys. Res. Solid Earth*, *119*, 2397–2414, doi:10.1002/2013JB010608.

Weijermars, R., and A. Poliakov (1993), Stream functions and complex potentials: Implications for the development of rock fabric and the continuum assumption, *Tectonophysics*, *220*, 33–50.

Weijermars, R., and H. Schmeling (1986), Scaling of Newtonian and non-Newtonian fluid dynamics without inertia for quantitative modelling of rock flow due to gravity (including the concept of rheological similarity), *Phys. Earth Planet. Int.*, *43*, 316–330.

White, F. M. (2011), *Fluid Mechanics*, McGraw Hill, New York.

Wörner, G., R. S. Harmon, J. Davidson, S. Moorbath, D. L. Turner, N. McMillan, C. Nye, L. Lopez-Escobar, and H. Moreno (1988), The Nevados de Payachata volcanic region (18°S/69°W, N. Chile). I. Geological, geochemical and isotopic observations, *Bull. Volcanol.*, *50*, 287–303.

Zill, D. G., and P. D. Shanahan (2009), *A First Course in Complex Analysis With Applications*, 2nd ed., Jones and Bartlett, Boston, Toronto, London, Singapore.

©2014. American Geophysical Union. All Rights Reserved.